Low-velocity out-of-plane impact tests on double-wythe unreinforced brick masonry walls instrumented with optical measurements

Michele Godio, Mathias Flansbjer, Natalie Williams Portal

PREPRINT VERSION ● 25.08.2022

Slow-velocity out-of-plane impact tests on double-wythe unreinforced brick masonry walls instrumented with optical measurements

Michele Godio *, Mathias Flansbjer , Natalie Williams Portal

RISE Research Institutes of Sweden, Brinellgatan 4, 504 62 Borås, Sweden

ABSTRACT

Unreinforced brick masonry makes up today a significant piece of the European built environment, including not only residential buildings but also strategically important structures that are not designed to withstand blasts and impacts. Yet, it is difficult to accurately estimate the response of these structures and the extent of damage they sustain during such extreme loading conditions. This paper presents the implementation and discusses the results of laboratory impact tests conducted on natural-scale double-wythe unreinforced brick masonry walls, a typology that is frequently found in Northern Europe. The walls were spanning vertically between two reinforced concrete slabs and were subjected to slow-velocity drop-weight pendulum tests in which they were repeatedly hit until the opening of a breach in the center of the wall. The tests were instrumented with both hard-wired and optical measurements, the latter consisting of high-speed cameras and digital image correlation techniques, to face the difficulty of observing cracks and determining the deflections of the walls with adequate accuracy at the time of the impact. Investigated in these tests were the out-of-plane response of the walls and their capacity to resist the impacts. The axial load applied on the top of the walls was varied for two wall configurations and monitored throughout the tests to study the effect of arching on the failure mechanism produced and number of repeated hits needed to open the breach. Of interest was also the evidence of cracking, more specifically the way it initiated on the undamaged walls and next propagated upon consecutive hits. The data generated from these tests are made available to support further investigations on unreinforced masonry structures subjected to extreme actions.

Keywords: Impacts; Masonry; Out-of-plane; Arching; Digital Image Correlation (DIC); High-speed cameras

1. Introduction

Unreinforced masonry (URM) walls have limited resistance to impacts and blasts, owing to the low tensile strength of the mortar and the brick-mortar interface. As such, the permissible deformation of the walls must be limited in order to avoid failure, which is especially true for loadbearing walls in structures and building facades. However, knowledge of the impact and blast resistance of loadbearing masonry walls is scattered and must be expanded. Interest in this

* Corresponding author: michele.godio@ri.se

topic is still relatively scarce in the literature, having grown only in the last ten years [1–3]. This upsurge in masonry structures is justified by the international socio-political context, in which practitioners are increasingly being asked to face the threat of attacks on civil structures and monuments [4].

Brick masonry was a popular construction material in Sweden in the nineteenth century, and in Northern Europe in general, until the first part of the twentieth century. As a result, masonry today makes up a significant section of the Swedish built environment, including monuments, churches, railroad stations, and other strategically important structures that were not designed to withstand the strains imposed by such harsh loading conditions.

Precisely assessing the response and the level of damage suffered by masonry during impacts and blasts is very challenging. Contrary to the static actions exerted by serviceability loads or settlements, or the dynamic actions generated by the wind or seismic events, which operate at relatively low strain rates, the actions generated by impacts and blasts involve high to ultra-high strain rates [3]. It is known that, when high-rate strains occur, the material response, notably its stiffness and strength, changes [5,6]. Unclear yet, is the way locally failure occurs, cracking initiates and develops, and strain waves propagate within the masonry at such high strain rates. Moreover, arching actions are key in this framework, as they lead to an increase in capacity for the walls. Instrumented experimental tests are therefore needed to characterize the response, both at the material and structural level.

The present study investigates these research questions by performing experimental tests that involve natural-scale URM walls subjected to slow-velocity impacts. Double-wythe walls were built by using red clay bricks and hydraulic lime-based mortar, a masonry typology that is frequently found in historic buildings in Northern Europe. The walls were tested at the laboratory of Applied Mechanics at RISE Research Institutes of Sweden (Borås, Sweden). They were placed into a test rig specifically designed for that purpose and subjected to drop weight pendulum tests in which they were repeatedly hit until the formation of visible damage. The tests were instrumented with both hard-wired and optical measurements, these latter used along with high-speed cameras, to face the difficulty of observing cracks and determining strain measures at the time of the impact.

Pendulum-type impact tests are known to be optimal for brittle-fracture materials, as they can easily convey potential energy into impact energy. The literature on pendulum impact test on masonry components is nonetheless very narrow. Gilbert et al. [7] performed laboratory tests on 21 natural-scale URM parapets disposed horizontally to simulate vehicle protection barriers. The primary objective of the experimental programme was to investigate the failure mechanisms of the parapets, upon application of impact loads that were designed to be comparable in magnitude and duration to those resulting from a vehicle impact. An ad-hoc test rig incorporating a vertical drop weight and a rotating quadrant arrangement was used to deliver the impact force horizontally against the walls' face. Many different wall configurations were tested, and the analysis of the mechanisms was further developed [8].

Investigated through this experimental campaign is the response to slow-velocity impacts of URM walls spanning vertically between two reinforced concrete (RC) slabs. The walls were tested in a vertical position for gravity to act in the right direction. Different pendulum

configurations were first tested. Next, the axial load applied on the top of the walls was varied and monitored throughout the tests to study the effect of arching on the failure mechanism and number of repeated hits needed to open a breach into the wall. Of interest was also the evidence of local deformation, with a focus on crack initiation and propagation. High-speed (HS) cameras used in conjunction with the Digital Image Correlation (DIC) method tracked closely the state of deflection and deformation of the walls at every instant during and after the impact.

Recent advances in imaging instrumentation, lighting resources, computational power and data storage capacity have brought optical measurements to cover a wide spectrum of applications across different fields of experimental mechanics [9]. In this framework, DIC is a widely recognised method based on optical measurements, employing tracking and image-registration techniques to obtain very accurate measures of the 3D displacement and deformation field of a material [10]. Some of today's algorithms for the automated detection of cracks in masonry structures are based on results from DIC [11–13]. Moreover, when used with high-speed cameras, the DIC method, hereafter indicated as HS-DIC, becomes a relevant tool in the understanding of the underpinning deformation process and cracking of quasi-brittle materials at high- to ultra-high-rate strains. Yet, its use in this field is at its early stage and limited to some construction materials like concrete [14] and structural glass [15]. In this study, the applicability of the HS-DIC method is proved on impact tests performed on natural-scale brick masonry walls.

Applications of the DIC method to masonry structures under impact conditions are, to the authors' knowledge, still unexplored, its use being limited to low-rate strains, that is for static loads [16–24] and those generated by earthquakes and traffic [25–27]. In blast tests, HS cameras have been uniquely used to observe the wall response in post-blast surveys, while deflections and strains were still measured by contact sensors like LVDTs and strain gauges [3]. This holds true for impact tests. In [7], most of the walls were instrumented with conducting paint crack detectors to collect evidence of cracking. However, because sensors provide point-wise information of the state of deflection and deformation of the walls, information on the local behaviour of mortar and brick-mortar interface is difficultly accessible by these means. In contrast, the emerging DIC techniques offer a versatile non-contact solution that allows the displacement field and cracking to be determined over the entire range of points covered by the image. This study proves the applicability and validate the use of these methods in laboratory conditions, more particularly on tests made on structural components. The experimental methodology developed here is general, and it can thus be applied to various setups, geometries, and loading conditions. Finally, the data generated in this experimental campaign lay the groundwork for the development and validation of advanced numerical models for URM structures subjected to extreme actions.

The paper is organized as follows. Section 2 describes the test units. Section 3 presents the tests performed to characterize the material properties. Section 5 introduces the test programme, while Section 4 explains the test setup. Section 6 contains a detailed description of the instrumentation used. Sections 7 and 8 incorporate the test results. Section 9 closes the paper.

2. Test units

Three URM walls were tested as part of the experimental programme (Fig. 1). The walls had nominal height, width, and thickness of about 1535 × 775 × 245 mm (Fig. 2). The actual walls'

dimensions are listed in Table 2. They were built as part of a larger experimental campaign including the characterization of the static out-of-plane behaviour of unreinforced masonry [28]. In total, 14 natural-scale walls were built, including single and double-wythe walls. Out of the double-wythe walls, 3 were tested here against impacts. These walls are denoted as W9, W10 and W11.

(a) (b) (c)

Fig. 1 Test units under construction (a); side view on Flemish brickwork (b); the test units after being tested (c).

2.1. Bricks

The choice of the construction materials was motivated by the estimated construction time of loadbearing masonry walls in Sweden (pre-1940's). The test units were built using Swedish standard solid red clay bricks, with nominal dimensions of 250 × 120 × 62 mm. The actual dimensions were measured and appeared to be 245 × 115 × 62 mm. The bricks were laid to form a regular pattern, with alternated stretchers and headers following a periodic Flemish-bond pattern, which required a skilled operator to build. The use of this specific brickwork, despite its name, already appeared in scattered areas of Northern and Central-East Europe on late medieval buildings.

2.2. Mortar

Both head (vertical) and bed (horizontal) joints were filled with hydraulic lime-based mortar of class CS I (D), with maximum aggregate size ≤ 1 mm, and aggregate-to-binder ratio of 1:1 to 4:1 (Combimix's Hydrauliskt Kalkbruk, KKh). This mortar is used nowadays mainly for rendering purposes and is expected to have better mechanical properties and workability than the pure lime-based mortar that can be found in historic buildings. Hydraulic mortar is however more practical, because it can harden in both air and water and can nevertheless be used in humid environments as it is breathable [29]. The joint thickness was maintained relatively constant in the walls and around an average of 10.5 mm for the bed joints and 14 mm for the head joints.

2.3. Reinforced concrete slabs

In all tested wall specimens, RC slabs were affixed below and over the walls to simulate the realistic contact conditions that can be found in existing buildings. The RC slabs had dimensions

980 × 500 × 75 mm (width × depth × height), see Fig. 2. Concrete of the type C25/30 was used, and two layers of steel reinforcement mesh were included in each slab. Four holes of diameter 22 mm were created at the corners of the top slabs, while four threaded lifting anchors (M12 NEO-BTK) were affixed in the corners of the bottom slabs. In this way, it was possible to lift and transport the test units to the test setup by an overhead crane, limiting the possibilities of generating tensile stresses inside them.

3. Characterization tests

The walls were tested to impact 211 days after their construction. During the curing phase, the walls were left inside the laboratory, with smaller oscillations of temperature and humidity than the outdoor conditions. Characterization tests were carried out in parallel with the impact tests to derive the mechanical properties of bricks, mortar, and masonry considered as a composite material. The results of these tests are listed in Table 1.

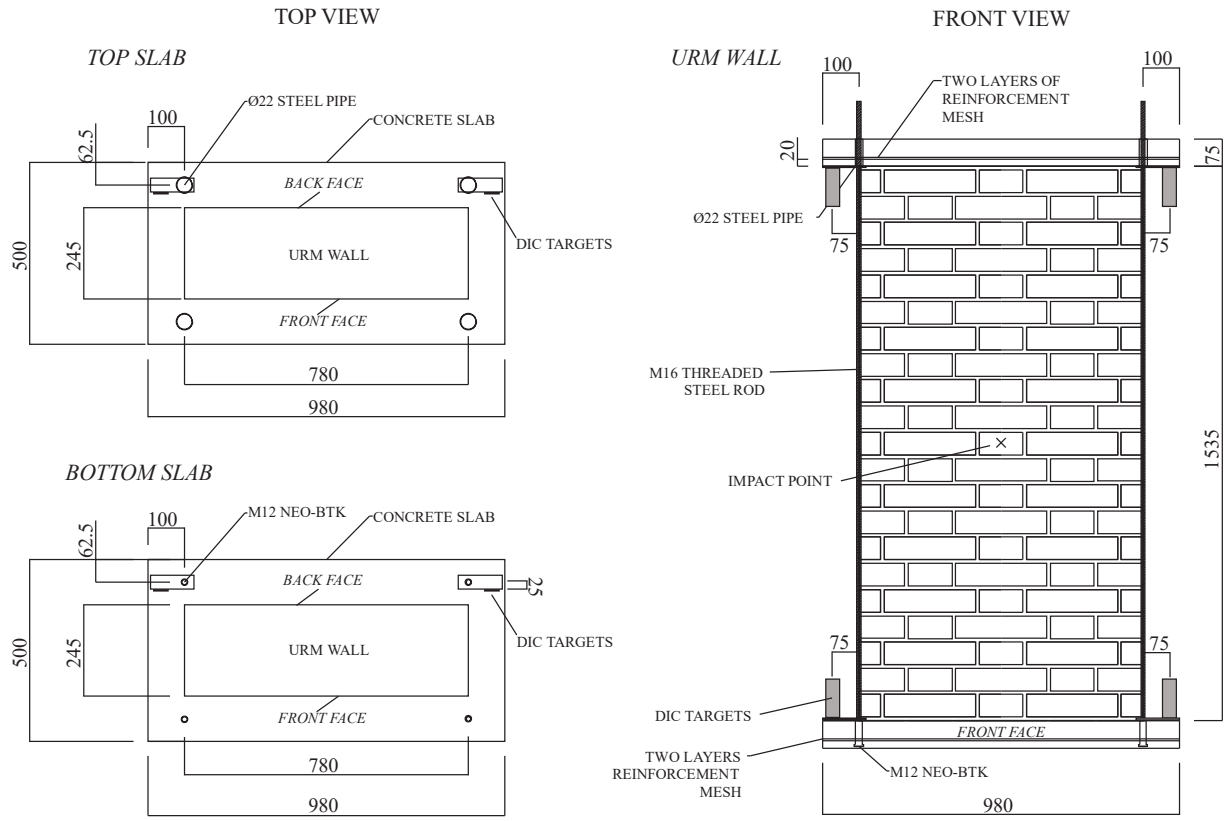

Fig. 2 Geometry of the test units.

3.1. Bricks properties

The compressive strength f_c of the brick was determined according to the EN 772-1 regulation [30]. The bricks were reduced to prisms of dimensions 150 × 100 × 60 mm by the saw and their surface was prepared (sanded flat). The samples were then conditioned by drying them in a heating cabinet at 105 ± 5°C and allowed them to cool in a climate room at 20°C and RF

50% four hours before they were tested. According to [30], the loading velocity was 0.6 MPa/s and a form factor of 0.75 was applied to the value obtained for the compressive strength. The density ρ of the bricks was determined following the specimen preparation. The flexural tensile strength f_t of the bricks was not determined.

3.2. Mortar properties

Tests for flexural and compressive strength of the mortar were performed 166-167 days after construction. The flexural tensile strength f_t of the mortar was measured following the EN 1015 regulation [31], on prisms of dimensions 100 × 40 × 40 mm that were sampled when constructing the walls. The density ρ was also measured at the time of the flexural tensile tests. The compressive strength f_c of the mortar was measured according to EN 1015 [31] on the halves resulting from the flexural tensile tests. From the manufacturer, the mortar was reported to have a compressive strength of 0.4-2.5 MPa after 28 days.

3.3. Masonry properties

A double-wythe wallet of size 514 × 390 × 245 mm was built and subjected to a uniaxial compression test [32] about 200 days after construction. The axial force was applied at the speed of 1.0 mm/min at the top of the wallet by means of a loading plate fastened to a hydraulic actuator of 1 MN of capacity. Another steel platen was placed at the bottom of the wallet. From the analysis of the failure mechanism, which is not reported here for brevity, it appears that the wall was laterally confined during the test, because of the friction forces developing between the wallet and the steel plates.

Table 1 Material properties resulting from the characterization tests on bricks, mortar and masonry.

Bricks		**Mortar**			**Masonry**	
ρ (kg/m^3)	f_c (MPa)	ρ (kg/m^3)	f_c (MPa)	f_t (MPa)	E (MPa)	f_c (MPa)
1715 ± 4 (0.2%; 6)	33.05 ± 0.69 (2.1%; 6)	1570 ± 7 (0.5%; 3)	0.85 ± 0.16 (18.3%; 4)	0.38 ± 0.03 (7.7%; 3)	2713 ± 564* (20.8%; 1) 4865 ± 1289** (26,5%; 20)	8.2 (0; 1)

Notation: mean ± standard deviation (C.o.V: coefficient of variation; number of samples tested).
* Value calculated according to EN 1052-1 [32]
** Value obtained by fitting unloading/reloading hysteresis cycles

Four unloading/reloading cycles were performed before reaching the peak force, at 0.5, 1.0, 1.5, 2.0 and 3.0 MPa. Then, the test was lead in monotonic way until failure of the axial loadbearing capacity of the wallet. Displacement field measurements were acquired by two 2D DIC measurement systems monitoring the front and back side of the specimen. Four virtual transducers measured the relative displacement over a base length that covered 2 units and 2 mortar layers. The compressive strength f_c was extracted by diving the maximum axial force by the cross section of the wall [32]. The modulus of elasticity E was extracted as the secant modulus from the measure of the strain at all four measuring positions, at a stress equal to 1/3 of the maximum stress achieved [32]. However, since initiation of cracking was observed for much

lower stress values (~1 MPa, i.e. about 1/8 of the maximum stress achieved), another method was used to derive E. This consisted in fitting the unloading/reloading cycles performed prior to reaching the peak force observed by the 4 virtual transducers [33].

The flexural tensile strength f_t of the masonry along the bed joints was not determined.

4. Test setup

The impact tests were conducted into a test rig that was designed specifically for this campaign. The weight impacting the wall was created by assembling in-house steel components.

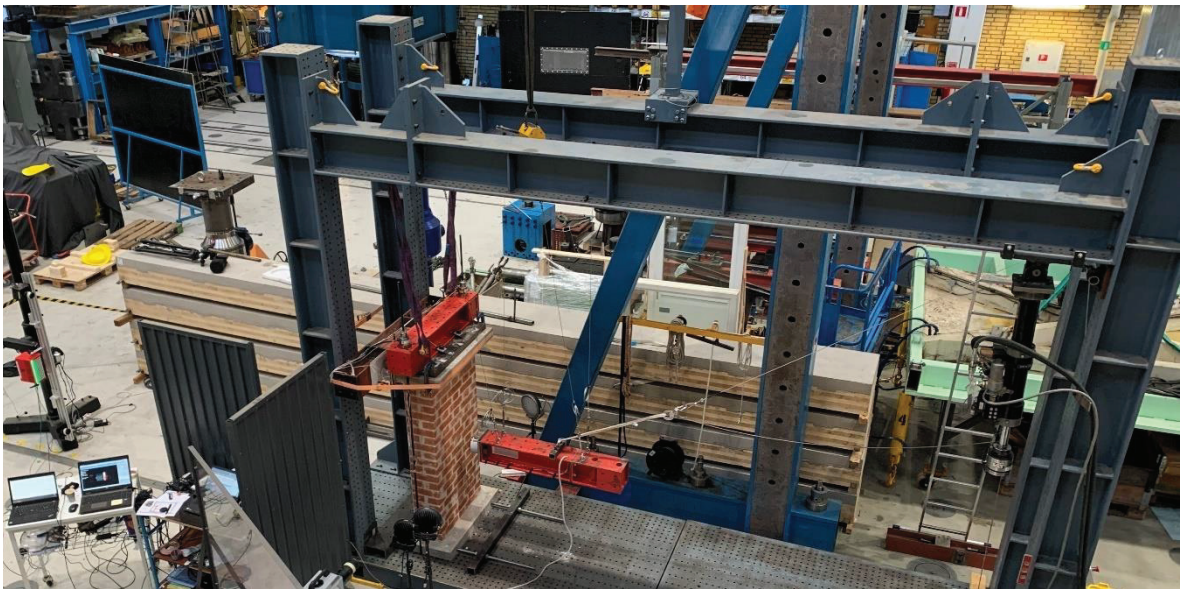

(a)

(b) (c) (d)

Fig. 3 Bird-eye view of the test setup and non-rigid supports (a). Side (b) and front (c) view of the URM wall. Lateral view on the drop weight (d).

4.1. Test rig

The test units were built outside the test stand and moved in for testing by an overhead crane. The rig consisted in two steel frames of height 3.5 m and length 5.0 m (Fig. 3). The frames were distanced by 1.2 m and mounted on a 220-mm thick steel floor which was, in turn, laid on the laboratory's strong floor. The two frames were connected by a 200 × 200 mm HEB steel beam, reinforced by 4 flanges, and placed transversally between the frames at 1.6 m from the steel floor (in brown in Fig. 3).

The support conditions put in place for the URM walls were designed to experimentally reproduce *non-rigid* boundary conditions for the walls. According to the definition given in [35] such conditions describe cases where the wall is supported by elastic supports and its resistance curve is therefore function of the supports' stiffness.

The lower RC slab was laid directly on the stand steel floor and pushed, by means of two threaded steel rods, against a 200 × 100 mm steel profile which ensured the force transfer between the slab and the base of the frame. The fixation system for the upper RC slab was designed to allow said slab to move vertically all while minimizing the occurrence of vertical friction forces and its rotation. To do this, the slab was pushed against the transversal beam and kept against it by a tie-down strap placed around the steel columns (in orange in Fig. 3). Two Teflon sheets and an interposed layer of grease were placed between the upper slab and the transversal brown beam.

A 50-mm thick steel loading platen was fastened to the top side of the upper RC slab; on the top of it, a 200 × 200 mm steel loading beam was fixed (in red in Fig. 3). Finally, an axial force was applied on the top RC slab through 2 lateral post-tensioned threaded M16 10.9 steel rods, connecting the loading beam directly to the steel floor. The rods were manually post-tensioned to the intended initial force before each drop. During the impacts, the rods could extend upon the walls' deflection, which resulted in an additional axial force applied to the walls, proportional to the rods elongation. The axial stiffness exerted by each rod was estimated to 15.7 kN/mm based on the rod properties.

4.2. Drop weight

The pendulum system was designed such that the drop weight kept its horizontal position during the free fall. Four cables connected the drop weight to the test rig (Fig. 3b). The impact occurred at the lowest point of the fall, with the impact force directed only in the horizontal direction. The drop weight hit the centre of the brick positioned at the 11th course from the top of the wall, in the exact middle of its surface (Fig. 3c).

As drop weight, we used an 800 × 200 × 200 steel HEB beam reinforced at its ends by two 15-mm thick steel flanges. At the end of the beam impacting the walls, a steel plate with an attached steel bulb was screwed (Fig. 3d). The bulb consisted of a steel cylinder with a hemispherical cap. In this basic configuration, the drop weight weighted 76.5 kg. To reach the final configuration of 116 kg, a short steel beam was attached at the other end of the beam.

5. Test programme

The experimental test programme consisted of 12 drop weight pendulum tests. The tests are listed in Table 2 as they were chronologically executed. The label given to each test, e.g. W*N*-*I*, refers to the wall specimen W of number *N* and the hit of number *I*. During the tests, the walls were subjected to repeated impacts until heavy damage was observed in the central part of the wall. We anticipate that none of the walls lost its axial loadbearing capacity because of the impact. In fact, although damage was heavy, the deformation was concentrated in the central part of the walls, thus not affecting their overall stability (Section 8).

All the walls were tested under the same support conditions. The first series of impacts were performed on wall W9 (test W9-1 to W9-5), which was used for exploratory tests on the definition of the impacting weight and drop height to be used in the two successive specimens. Two different heights were initially applied, 0.5 and 1.0 m, with an impacting weight of 76.5 kg. The weight was later incremented to 116 kg and dropped from 1.0 m. This final configuration, 116 kg from 1.0 m, was used for the walls W10 and W11. In tests W10-1 to W10-4 and tests W11-1 to W11-3, the walls were repeatedly hit with the same weight-height configuration until the occurrence of heavy damage, which roughly corresponded to the opening of a breach in the wall. A different axial load was applied on the top of these two walls, respectively 0.2 MPa for wall W10 and 0.05 MPa for wall W11, to study its influence on the failure mechanism and crack propagation throughout the hits, along with the number of repeated hits needed to open a breach.

Table 2 Test programme.

Test*	$H_w \times L_w \times t_w$ (mm)	Axial stress** (MPa)	Drop weight (kg)	Drop height (m)
W9-1	1535 × 775 × 245	0.2	76.5	0.5
W9-2	“	“	“	1.0
W9-3	“	“	116.0	“
W9-4	“	“	“	“
W9-5	“	“	“	“
W10-1	1535 × 775 × 245	0.2	116.0	1.0
W10-2	“	“	“	“
W10-3	“	“	“	“
W10-4	“	“	“	“
W11-1	1535 × 780 × 245	0.05	116.0	1.0
W11-2	“	“	“	“
W11-3	“	“	“	“

* All walls were tested under non-rigid support boundary conditions characterized by a support stiffness of 31.4 kN/mm.

** The value does not include the self-weight of the RC slab (95 kg), steel plate and loading beam (262 kg) affixed to the top of the walls.

In one test (W10-4), technical issues with the lighting system prevented the 3D HS-DIC measurements to be recorded during the test. Still, a single set of pictures was taken at the end of that test, to be able to correlate the end state of the wall and compare it with the previous

stages of the test (W10-1, W10-2, W10-3).

6. Instrumentation

The tests were instrumented with hard-wired and optical measurements. Analogue signals measured the force in the two post-tensioned rods, the strain in two points at about mid-height of each of the post-tensioned rods, and the acceleration in two points of the drop weight. One HS camera measured, by 2D DIC, the displacement, velocity and acceleration of the drop weight in the vicinity of the impact point with the wall. Two other HS cameras were used in stereo mode to obtain, through 3D DIC, field measurements of the back face of the wall, the one opposite to the one subjected to the impacts, and the support conditions.

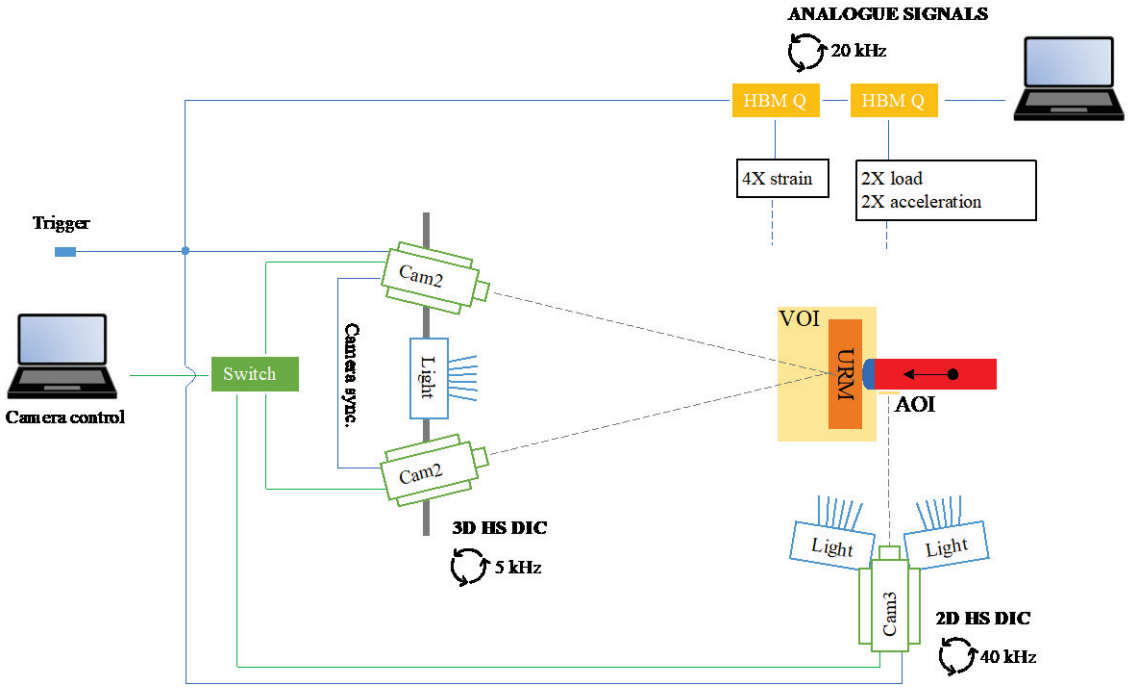

(a)

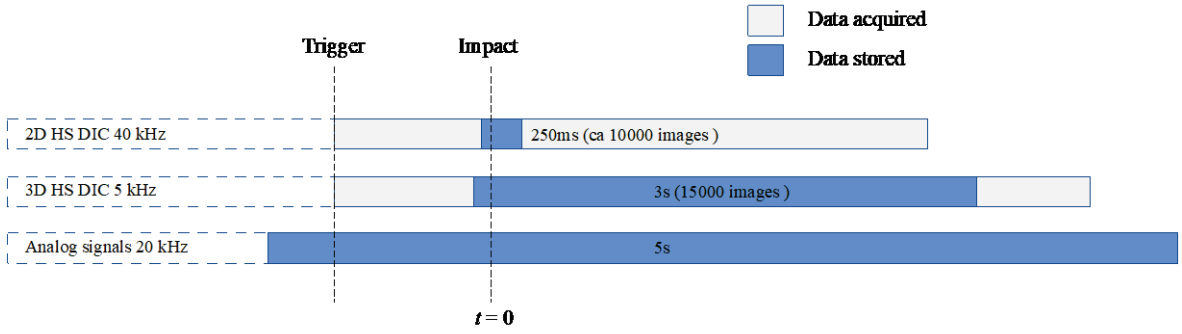

(b)

Fig. 4 Data acquisition (a) and time-synchronization (a) schemes between analogue signal and image acquisition systems.

6.1. Data acquisition systems

Two acquisition systems were used to collect data, one for the analogue signals, and one for the images recorded by the three HS cameras (Fig. 4). The image acquisition was started manually by a camera triggering system. The triggering signal was used as an input also in the analogue signal acquisition system, to enable time synchronization between both acquisition systems. The analogue signals were started before the triggering system was activated. In total, analogue signals were recorded for 5 s. The image acquisition system was started right before the impact of the drop weight and stopped automatically when the memory in the cameras became full. Not all the images acquired were stored, but only those belonging to a time window of interest for the impact analysis. In total, 10k images (corresponding to 250 ms) were stored for the 2D DIC measurement, and 15k pairs of images (corresponding to 3 s) for the 3D DIC measurement.

6.2. Analogue signal measurements

The analogue signals were acquired by a laptop computer by a data acquisition system consisting of HBM Catman software and HBM QuantumX measuring modules MX840 (force transducers and accelerometers) and MX1615 (strain gauges), with a sampling rate of 20 kHz. The analogue signal acquisition system was used to measure the force and strain in the post-tensioned rods, and the acceleration of the drop weight.

The axial force in each of the two rods was measured by 200 kN force washer transducers, placed around the rods on top of the loading beam. A spherical washer was placed between the force transducer and the tightening nut to ensure an even force distribution. The force transducers were used both before the tests, to apply the intended initial axial stress by post-tensioning, and during the tests, to measure the variation in the axial force during and after the impact.

The axial strain of the rods was measured by four strain gauges, two for each rod, positioned at the rod mid-height. Before testing, the rods were gently machined to remove the threads in order to get smooth surfaces where to glue the strain gauges. The strain measures were then used to derive the axial force in the rods, to be compared with the one measured by the force transducers.

Two accelerometers were positioned at the backside of the end flange of the beam used as drop weight, one at each side (left and right) of the beam web. The accelerometers were attached to the metallic surface of the beam by beeswax to get a good transmission and held in position by magnetic holders. The acceleration of the drop weight was calculated as the average value of two accelerometers. This acceleration was then used to derive the impact force.

6.3. 2D high-speed DIC measurements

The movement of the drop weight was monitored using the 2D DIC method with a Photron FASTCAM SAZ HS camera to determine its displacement, velocity and acceleration (Fig. 5a).

The camera was equipped with a 70-200 mm Nikon lens, with the focal length set at 200 mm and the aperture at *f*/4 during the test. The camera was placed at a perpendicular distance of about 1.9 m from the surface of the hemispherical bulb. A camera resolution of 1024 × 400 pixels and

an image acquisition rate of 40 kHz were used, corresponding to a time resolution of 0.025 ms. The camera configuration allowed for a field of view (area of interest) of approximately 223 × 87 mm^2, covering the bulb during the impact. The image spatial resolution and the corresponding field of view was determined by a reference scale. The speckle pattern was printed on self-adhesive paper that was attached to the cylindrical part of the bulb. To obtain high contrast levels of the pattern, the bulb was illuminated by two high-power led lamps.

The images were analysed by the DIC technique using the proprietary software package GOM Correlate. For each test, a sequence of 2500 images at the occasion of impact were selected for evaluation, corresponding to a time sequence of 62.5 ms. The dimensions of each subset were 30 × 30 pixels, and the subset step was 10 pixels, which corresponds to a subset size and data point spacing of approximately 6.5 mm and 2.2 mm, respectively. The displacement resolution was approximately 0.002 mm for both the x- and y-displacement components, determined as the standard deviation between static images of the pattern before loading. To minimize the measuring noise, displacement, velocity and acceleration were determined as average values of a surface including approximately 400 data points.

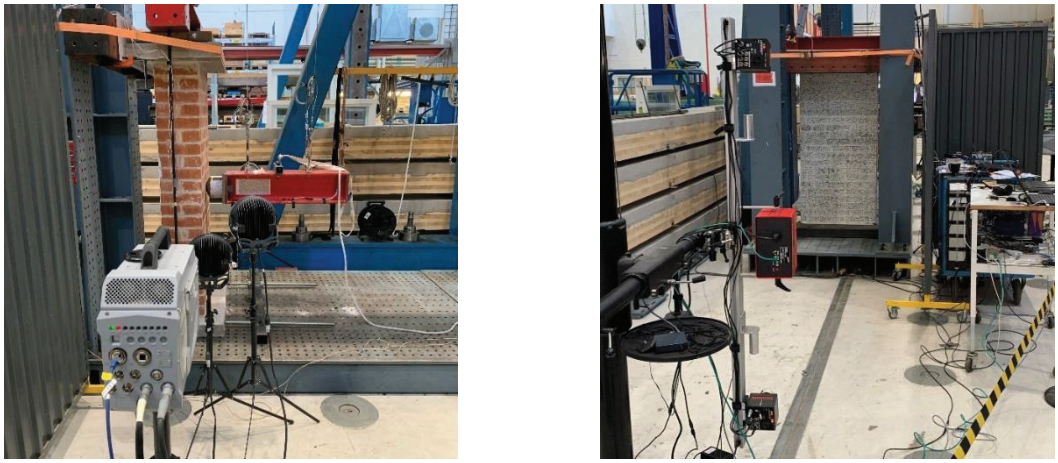

(a) (b)

Fig. 5 2D (a) and 3D (b) high-speed DIC measurement setups.

6.4. 3D high-speed DIC measurements

To analyse the dynamic response of the masonry walls to impacts, 3D DIC measurements based on a stereoscopic camera setup with two vertically arranged HS cameras were employed on the back side of the walls (Fig. 5b). The measurements were used to study the formation and propagation of cracking, along with the out-of-plane displacements and uplift of the walls.

Two Photron Mini AX100 cameras were mounted on a rigid aluminium profile with a relative distance of 1.7 m and angle of 24°. The camera setup was positioned at distance of approximately 4 m from the surface of the walls. On the cameras were mounted 50 mm fixed Nikon lenses and the aperture was set to *f*/4. An image resolution of 1024 × 720 pixels and an acquisition rate of 5 kHz were used, which corresponds to a time resolution of approximately 0.2 ms. The cameras were synchronized in time by connecting them with a synchronization cable and using a master-slave mode. Before testing, the system configuration was calibrated for a measuring volume of

approximately 1565 × 1120 × 1120 mm^3 (x, y, z), covering slightly more than the face of the wall. The speckle pattern used for the subset correlations was achieved by first applying white retro reflective paint as background and then black stains using a rough plastic brush. To obtain high contrast levels, during the tests the walls were illuminated by a high-power white LED light panel.

The movements of the top and bottom RC slabs, used to derive the wall uplift, were screened through 3D DIC by means of four small steel targets covered with white background and black speckle, secured on the upper and lower RC slabs, parallel to the back face of the walls and close to their corners (Fig. 2).

For each test, 1000 pairs of images, corresponding to 200 ms, were imported and analysed in GOM Correlate. To keep track of the cumulated damage, one image was imported before the first impact of each wall (W9-1, W10-1 and W11-1) and used as reference image in the evaluation of the following impacts. By doing so, deformations, cracks, etc., were related to the undamaged state of the wall prior to testing. The dimensions of each subset were 15 ×15 pixels, and the subset step was 10-pixel large. For the system configuration employed, this corresponds to a subset size and a data point spacing of approximately 23.3 mm and 15.5 mm, respectively, at the surface of the wall. The displacement resolution was determined to approximately 0.015 mm for both the x- and y-displacement components and approximately 0.050 mm for z-component, determined as the standard deviation between static images of the pattern before loading.

7. Impact analysis

The results of the pendulum impact tests are presented in this section and in Section 8. The observation of the test results indicates that several subsequent impacts occurred between the drop weigh and the walls. Here we focus on the primary impacts because they transferred much higher energy than the consecutive ones. The time scale of all the records was shifted so that the primary impact occurs at $t = 0$ for all the measurements. This instant was determined by eye, after observation of the drop weight velocity obtained by the 2D HS-DIC (Section 7.1).

7.1. Drop weight kinematics

Fig. 6 displays the horizontal and vertical displacements of the drop weight recorded for about 60 ms around the impact, while Fig. 7 displays its horizontal velocity. These measurements were obtained by the 2D HS-DIC optical system, as described in Section 6. The horizontal and vertical displacements were considered positive when indicating, respectively, a movement towards the surface and the top of the wall (the sign convention for velocity and acceleration followed accordingly). Both measures were shifted in order to have a value of 0 mm for $t = 0$.

Focusing on the horizontal displacement, in all tests, the drop weight bounced after the impact with the face of the wall, as indicated by the change in slope (resp. in sign) of the displacement-time (resp. velocity-time) records. The peaks in the displacement-time records correspond to the instant when the drop weight reached zero velocity and started bouncing back. The instant at which this occurred, t_{bounce}, and the corresponding displacement, d_{bounce}, are listed in Table 3.

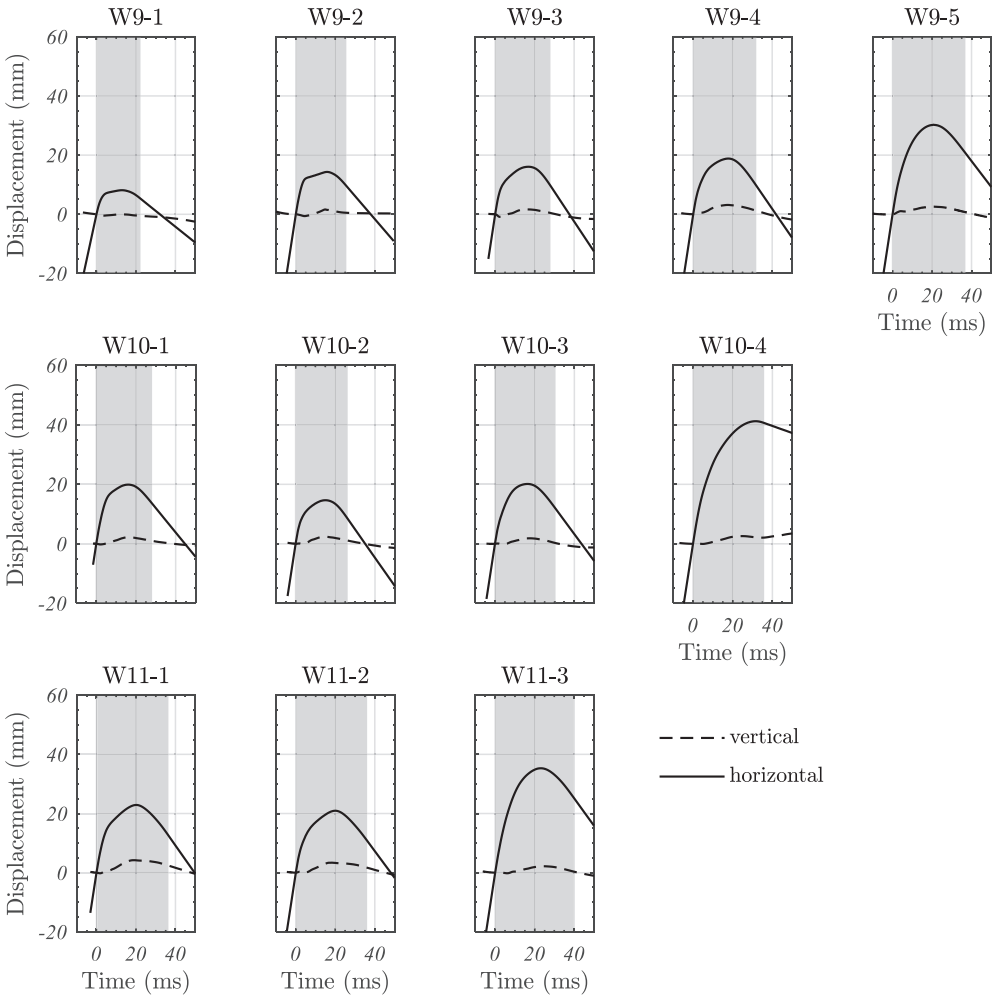

Fig. 6 Horizontal and vertical displacements of the drop weight. Source: 2D HS-DIC measurements. Legend: gray-shaded areas indicate the interval when the impact occurred.

Included in the table are the impact duration, Δt_{imp}, which was obtained as the difference between the instant when the drop weight lost its pre-impact velocity, v_{pre}, for the first time, and that when it started bouncing back freely at the post-impact velocity, v_{post}. The pre- and post-impact velocities were related by the drop weight mass M_{dw} to the momentum $P_{\mathrm{pre}} = M_{\mathrm{dw}} v_{\mathrm{pre}}$ and $P_{\mathrm{post}} = M_{\mathrm{dw}} v_{\mathrm{post}}$, whose difference is indicated with ΔP and equals the impulse I recorded on the drop weight during the impact (Table 3).

The vertical displacement of the drop weight was nearly zero before the impact, while it increased after the drop weight has hit the wall. This uplift is the result of the circular free-fall trajectory followed by the drop weight. It is visibly small compared to the horizontal displacement and it tends to vanish with the bouncing back of the drop weight.

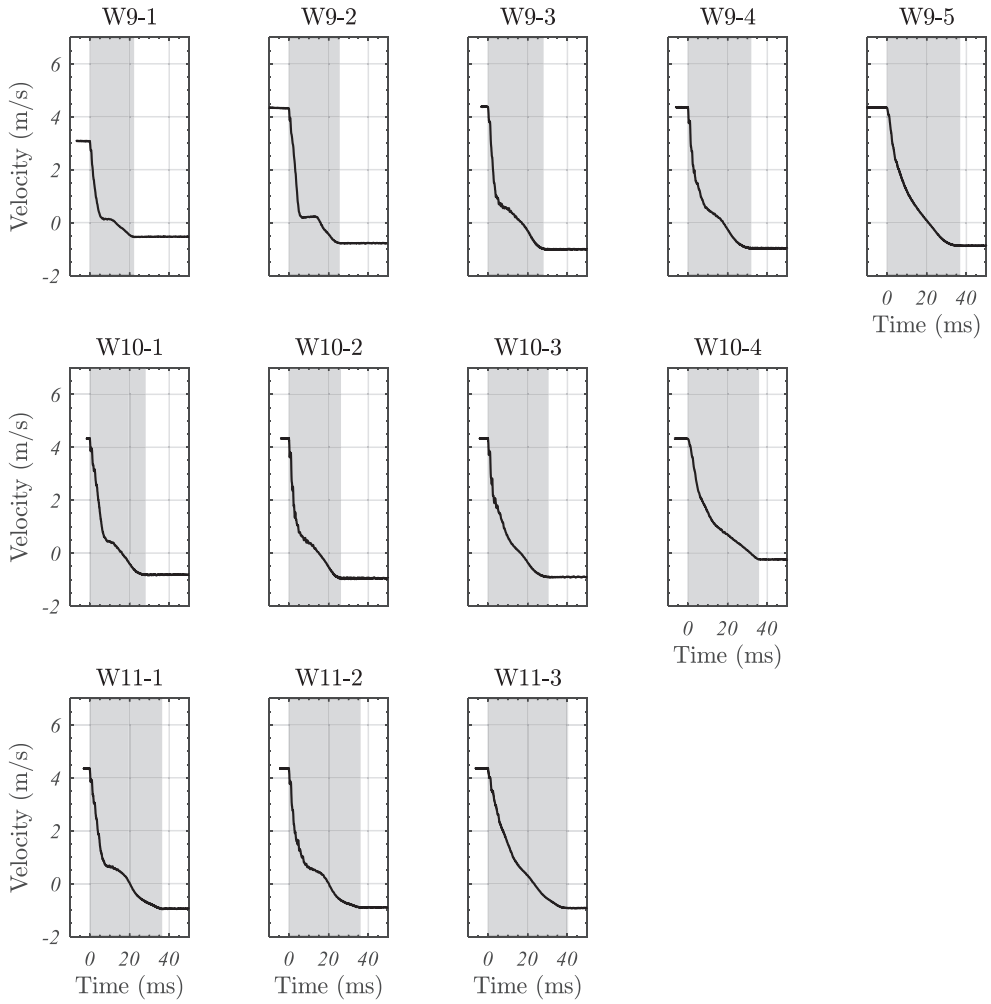

Fig. 7 Horizontal velocity of the drop weight. Source: 2D HS-DIC measurements. Legend: gray-shaded areas indicate the interval when the impact occurred.

7.2. Impact force

The impact force was derived by multiplying the mean of the acceleration-time records obtained by the two accelerometers that were installed on the drop weight by the mass of the latter. Fig. 8 displays the resulting records, which are illustrated here with positive sign to indicate the force exerted by the drop weight on the wall.

The peak force, Q_{peak}, and the instant at which this occurred, t_{Q}, were extracted from the records and are included in Table 3. Two distinct peaks were observed in the test W9-2. This seems to be due to the impact of the drop weight on the wall surface, which occurred gradually because of the slight inclination that affected the object at the end of the free-fall (see the vertical displacement in Fig. 6). Two major peaks could also be observed for W10-1, W11-1. For these walls, the impact appeared to occur instantly and the presence of two peaks could be related to the visible formation of cracking around the impact point (see Fig. 10-Fig. 12 and section 8.1).

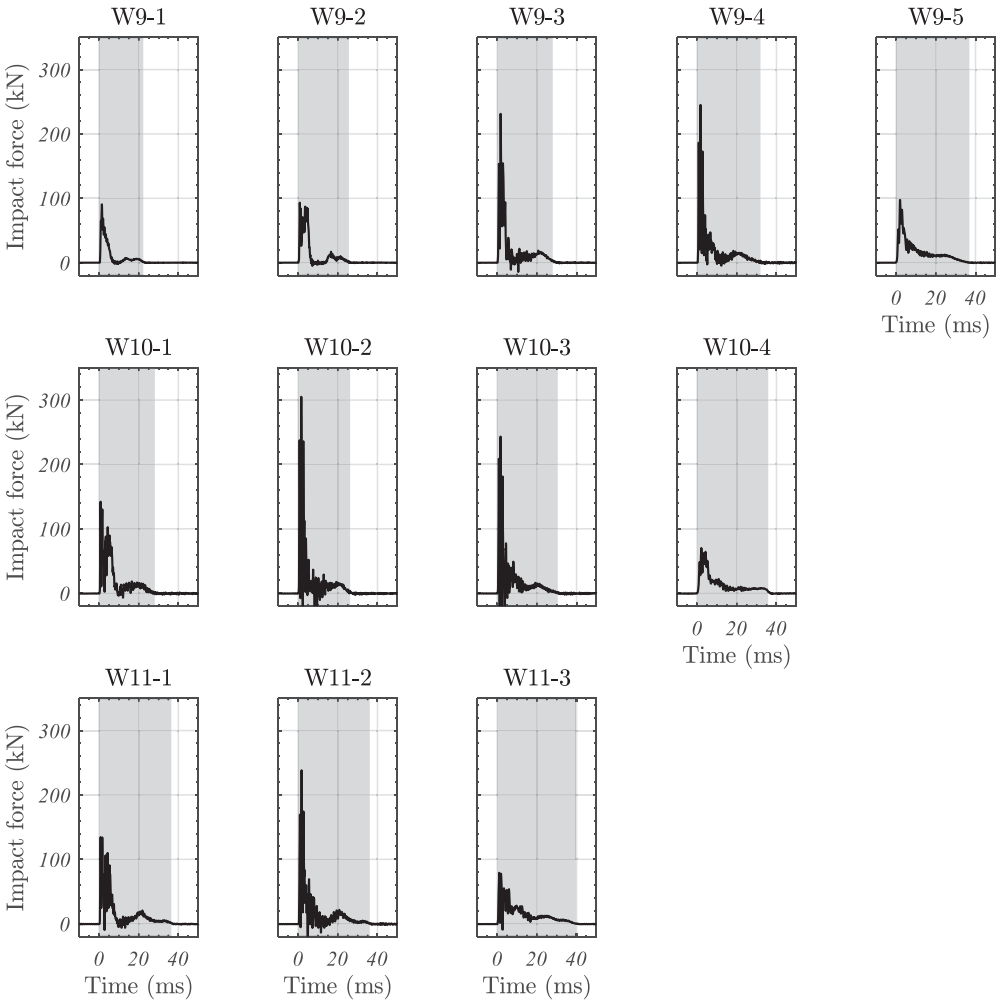

Fig. 8 Horizontal impact force. Source: accelerometers, mean value. Legend: gray-shaded areas indicate the interval when the impact occurred.

Acceleration-time records were also extracted from the 2D HS-DIC optical system. In Appendix A those signals are analyzed and compared to those given by the accelerometers, from which the impact force represented in Fig. 8 was derived, showing how the optical measurements can be used as a valid alternative to hard-wired measurements when recording the impact force.

7.3. Discussion of the results

The pre-impact velocity, v_{pre}, was compared to the theoretical values for the free-fall pre-impact velocity, which were calculated based on the drop weight configurations (Table 2), yielding an error of less than 3% for all tests. Similarly, the impulse I could be calculated upon integration of the force-time history recorded during the impact (Fig. 8) and compared with momentum difference, ΔP, derived from the velocity records (Fig. 7). The comparison yields an error smaller than 2.7% for all tests. The comparison is reported in Appendix A where the error is calculated for the force records derived by the 2D HS-DIC. The error is in the latter case

comparable to the former, which assures the accuracy of the optical measurements in characterizing the impact.

Fig. 9 complements the impact analysis by grouping the quantities contained in Table 3 for each of the tested walls. The damage cumulated in the walls due to the repeated hits entails longer impact durations Δt_{imp} (Fig. 9a). This holds true for all the walls; the change in impact configuration tested on the wall W9 (W9-1 to W9-3) yields the same effect. In addition, an increase of axial load (c.f. W11 with W10) provides an additional stiffness to the wall, which results in a relatively shorter impact. The peak force is reached for all tests at the very early stages of the impact, $t_{\text{Q}} = 0.02\text{-}0.06\Delta t_{\text{imp}}$ (Fig. 9b), while the drop weight is arrested and started bouncing back much later, $t_{\text{bounce}} \approx 0.60\,\Delta t_{\text{imp}}$ (Fig. 9c). Repeated hits lead the walls to increasing out-of-plane displacement or deformation, which results in an increase of drop weight maximum displacement d_{bounce} (Fig. 9d). Furthermore, an increase of axial load appears to increase the strength of the wall and its capacity to limit the drop weight displacement (c.f. W11 with W10).

Table 3 Characterization of the impacts resulting from the pendulum tests.

Test	Δt_{imp} (ms)	t_{bounce} (ms)	d_{bounce} (mm)	t_{Q} (ms)	Q_{peak} (kN)	v_{pre} (m/s)	v_{post} (m/s)	P_{pre} (kg m/s)	P_{post} (kg m/s)	ΔP (kg m/s)
W9-1	22.3	12.9	8.1	1.4	90.6	3.08	-0.54	235.6	-41.4	277.0
W9-2	25.6	15.9	14.3	0.8	93.1	4.34	-0.78	331.8	-59.8	391.5
W9-3	28	17	16.1	1.7	231.2	4.36	-1.01	506.0	-117.4	623.5
W9-4	32	17.7	18.8	1.7	245.1	4.35	-0.96	504.0	-111.6	615.7
W9-5	36.9	20.8	30.2	2	97.5	4.33	-0.86	502.2	-99.6	601.8
W10-1	28.1	16.1	19.9	0.8	142.1	4.3	-0.82	498.2	-94.6	592.9
W10-2	26.2	15.1	14.6	1.6	305.1	4.36	-0.94	505.7	-109.5	615.1
W10-3	30.5	16.4	20.1	1.7	243.2	4.34	-0.90	503.8	-104.3	608.1
W10-4	35.9	31.6	41.2	2.1	70.1	4.32	-0.27	500.8	-31.0	531.8
W11-1	36.5	20.2	22.9	0.8	134.4	4.37	-0.95	507.4	-109.7	617.1
W11-2	36.1	20.1	20.9	1.7	238.3	4.33	-0.90	502.2	-105.0	607.1
W11-3	39.8	23.2	35.3	1	79.1	4.34	-0.92	503.2	-106.4	609.6

8. Wall response

The kinetic energy lost by the drop weight because of the impact was partially converted into kinetic and potential energy for the walls, resulting respectively in deflection and elastic deformation, and partially dissipated by the cracking and crushing of the masonry. Of interest, here, are the observed failure mechanisms, the way cracking initiated and propagated inside the material during the impact, the out-of-plane displacements (deflections) of the wall, and the uplift of the wall at its top support and the arching action inside it.

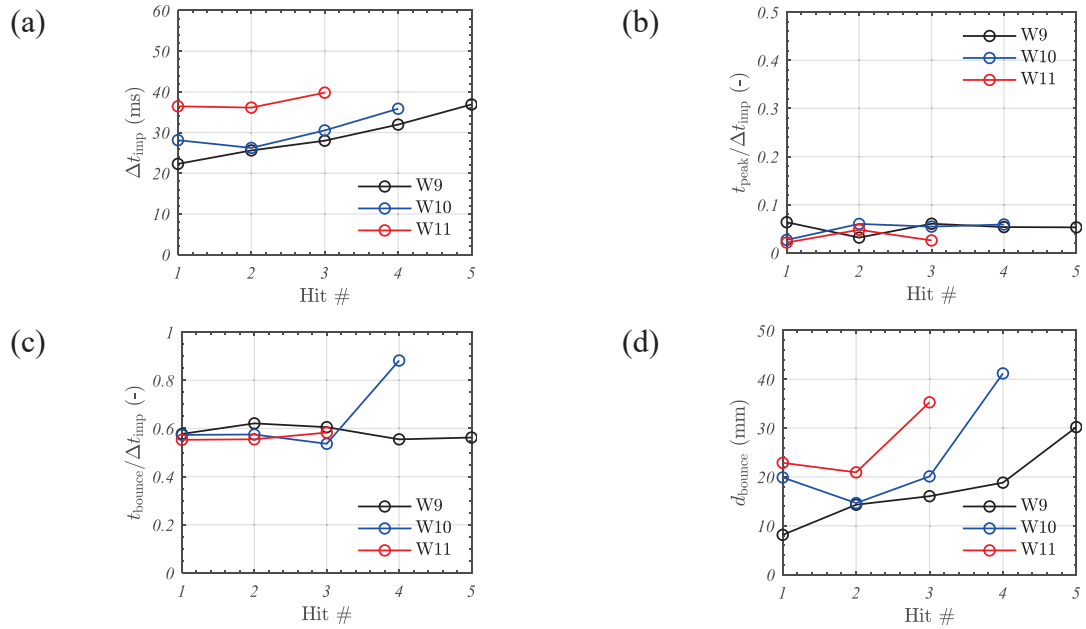

Fig. 9 Characterization of the impacts for each of the tested walls W9, W10, W11. The values displayed are contained in Table 3.

8.1. Formation of failure mechanisms

Fig. 10-Fig. 12 show the maps of major technical strain, ε_I, that developed on the surface of the undamaged walls at different instances of the tests W9-1, W10-1, W11-1. The plots were produced after processing the results obtained via the 3D HS-DIC optical system employed on the back face of the walls (Section 6). The major strain is used here to qualitatively locate the cracked regions of the walls, as a proxy for more sophisticated crack detection algorithms [12].

Two types of failure mechanisms can be individuated starting from the observation of the crack patterns: the overall deflection of the walls on one hand, and the punching of the walls by the drop weight on the other. These mechanisms were observed for all walls and the observations were corroborated by the study of the out-of-plane displacements, showed in Fig. 13-Fig. 15 and considered positive when in the direction of the impact.

The former mechanism corresponds to the vertical spanning of the wall and resulted in a major horizontal crack dividing the wall into separate blocks; the crack is located between the 6th and 7th course of bricks in wall W9, and between the 10th and 11th course in walls W10, W11. The latter mechanism produced localized damage at the mid-height of the wall. Not only it produced heavy damage around the middle brick, which was punched by the drop weight (Fig. 13-Fig. 15), but it also generated significant out-of-plane brick dislocations in the area surrounding said brick (Fig. 10-Fig. 12). The areas where such dislocations occurred extends from 1-2 courses above to 1-2 courses below the middle brick. They are characterized by stepped diagonal cracks, along with an overall horizontal spanning of the wall, the wall being not laterally supported in that region. These areas were particularly visible for the most damaging impact configuration, which was experienced in the test W11-1 (Fig. 12, Fig. 15).

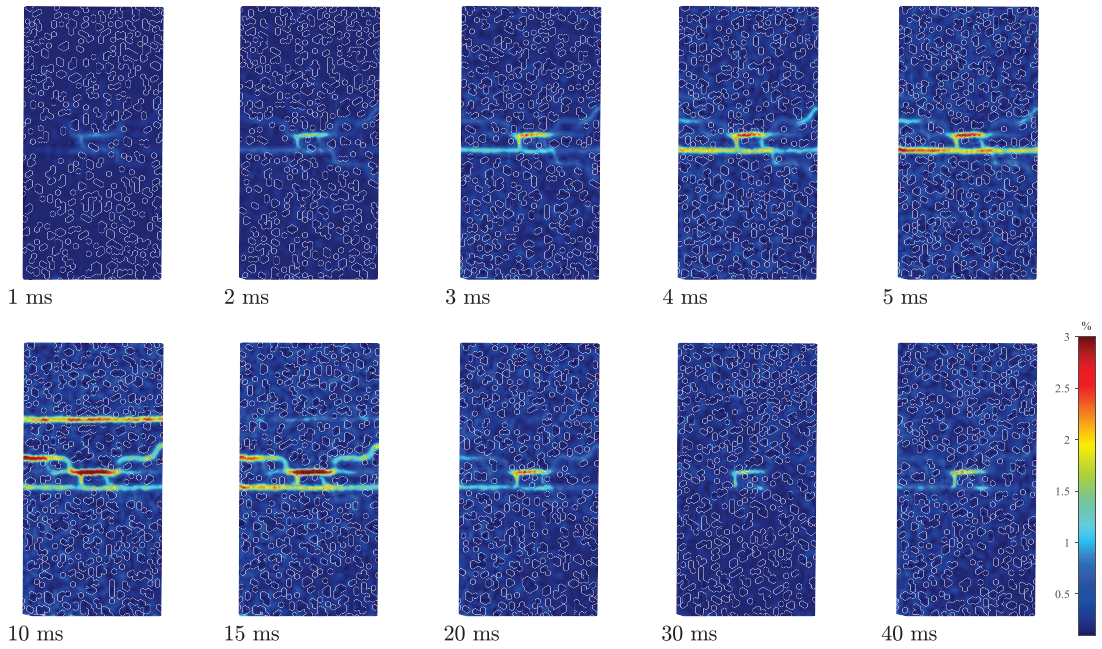

Fig. 10 Major strain of the back face of the walls at different instances of the pendulum tests. Test W9-1. Source: 3D HS-DIC measurements.

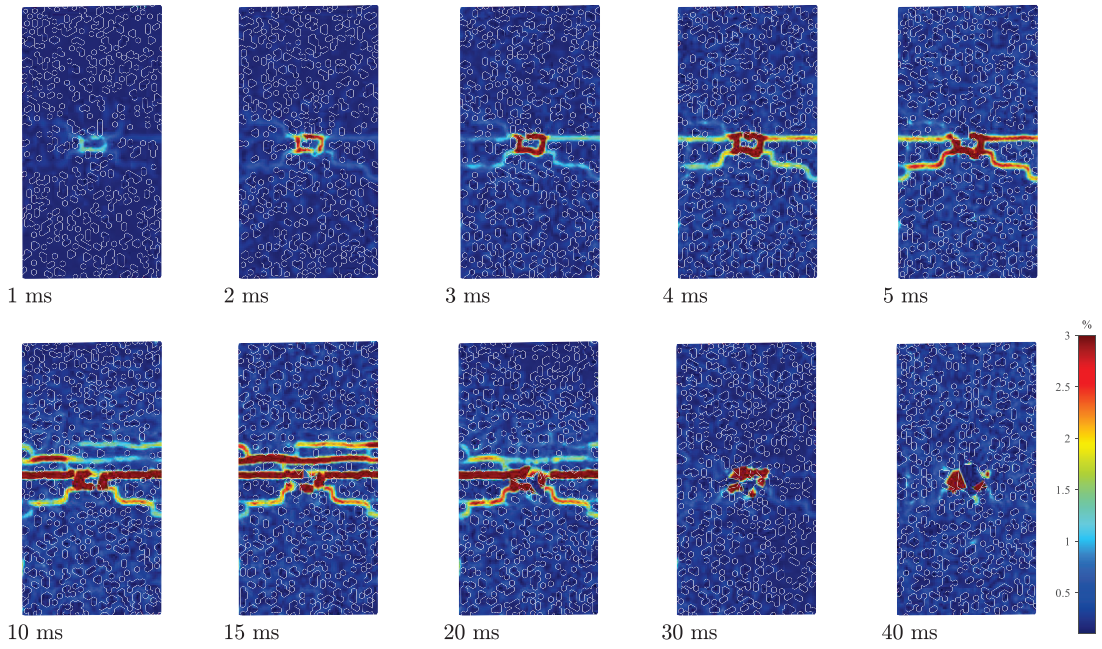

Fig. 11 Major strain of the back face of the walls at different instances of the pendulum tests. Test W10-1. Source: 3D HS-DIC measurements.

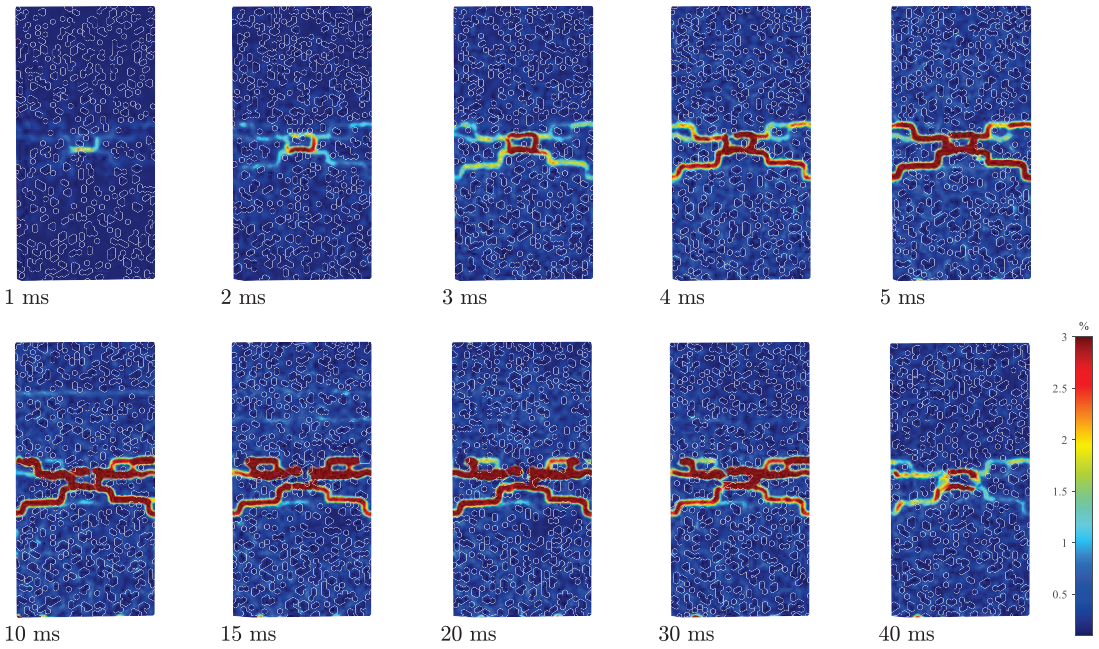

Fig. 12 Major strain of the back face of the walls at different instances of the test W11-1. Source: 3D HS-DIC measurements.

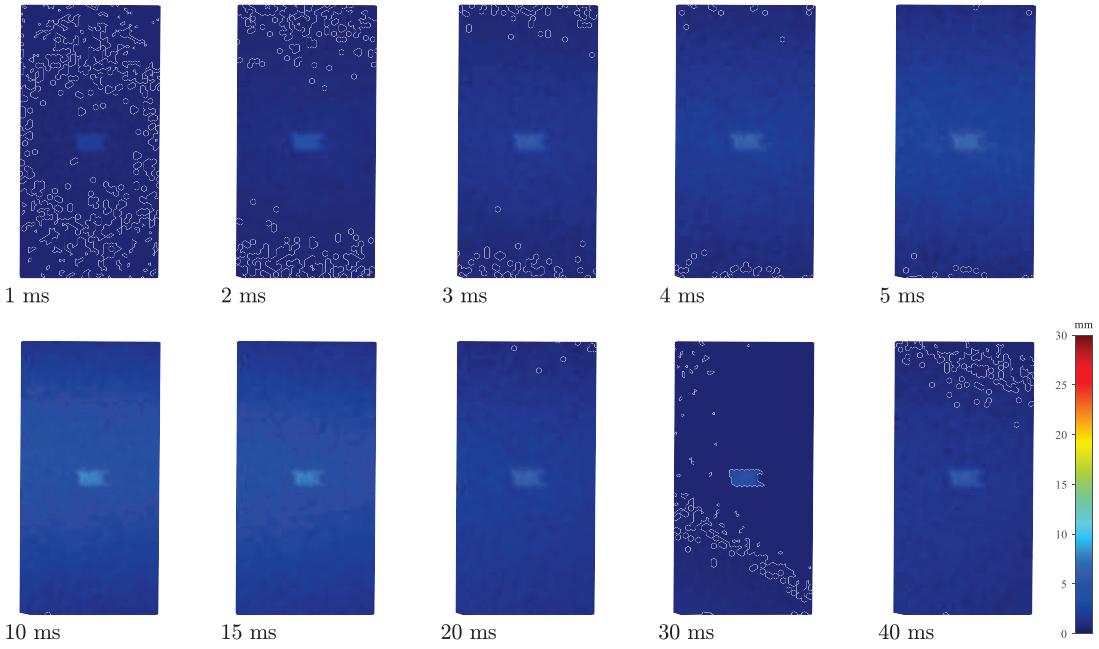

Fig. 13 Out-of-plane displacement of the back face of the walls at different instances of the test W9-1. Source: 3D HS-DIC measurements.

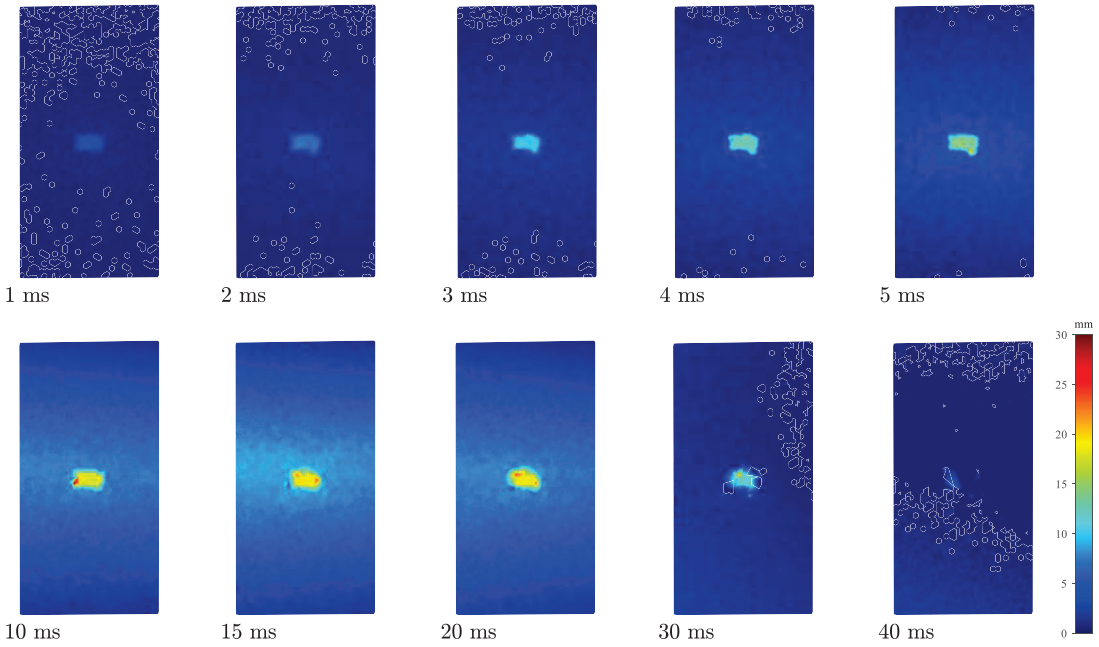

Fig. 14 Out-of-plane displacement of the back face of the walls at different instances of the test W10-1. Source: 3D HS-DIC measurements.

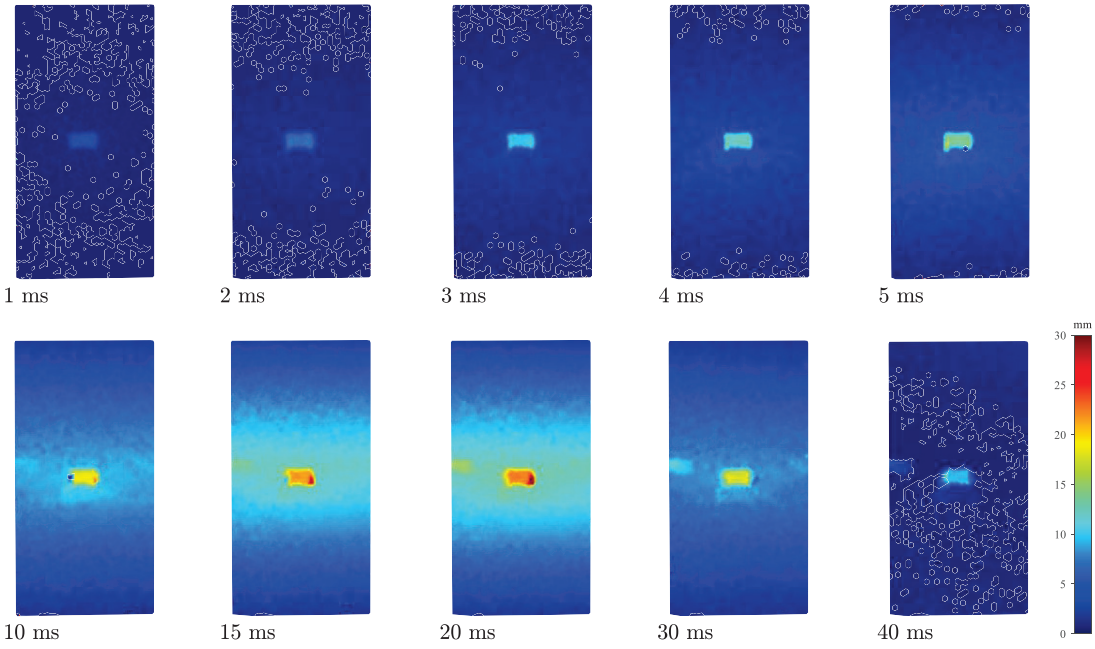

Fig. 15 Out-of-plane displacement of the back face of the walls at different instances of the test W11-1. Source: 3D HS-DIC measurements.

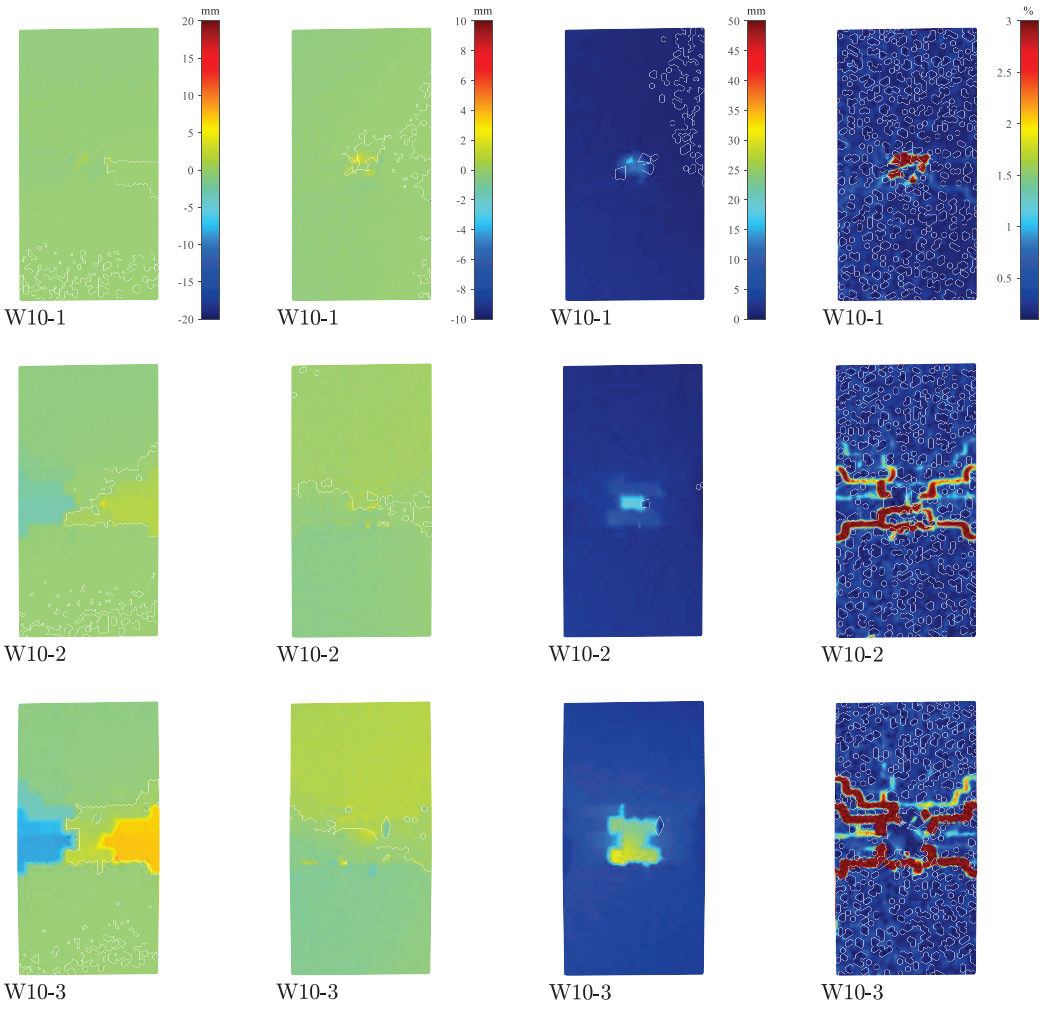

Fig. 16 From left to right: in-plane horizontal displacement, in-plane vertical displacement, out-of-plane displacement, and major strain of the back face of wall W10 upon consecutive tests at 30 ms. Source: 3D HS-DIC measurements.

8.2. Propagation of cracking during impacts

Fig. 10-Fig. 12 show that the cracks on the back face of the undamaged walls initiated directly behind the impact point, and later propagated remote from this point. This holds true especially for the cracks generated inside the region where dislocations occurred. On the contrary, the major horizontal cracks that formed upon wall deflection could originate far from said region, as in the case of wall W9, because of the attainment of a critical wall deflection, stretching the outermost fiber beyond the tensile strength.

The maximum extent of cracking reached in the walls generally occurred approximately when the peaks of the applied impact force were observed (c.f. Fig. 8). Not visible from the figures are the cracks occurring between the first and last course of bricks and the adjacent RC slabs. Those cracks were detected by eye at the end of each test, see Section 8.4. It is believed that those

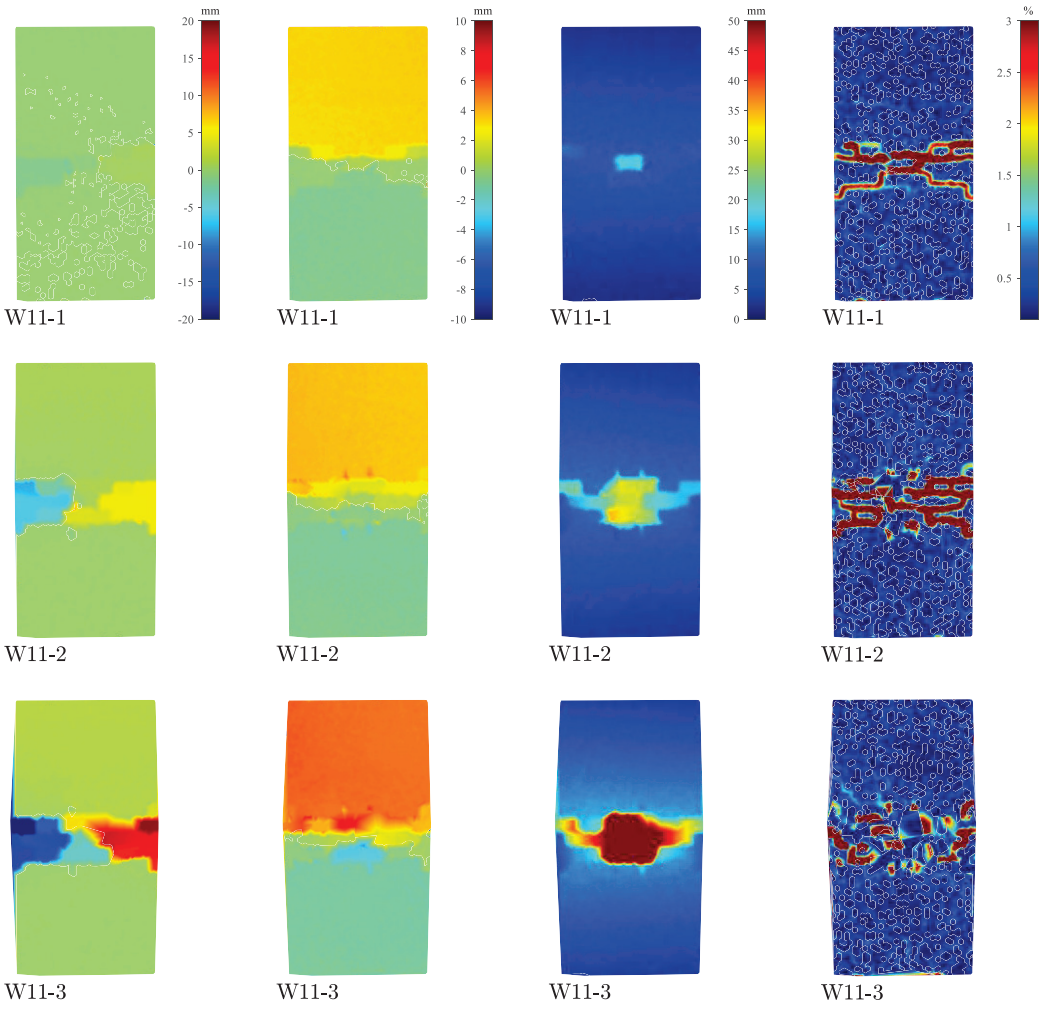

Fig. 17 From left to right: in-plane horizontal displacement, in-plane vertical displacement, out-of-plane displacement, and major strain of the back face of wall W11 upon consecutive tests at 30 ms. Source: 3D HS-DIC measurements.

cracks formed approximately at the same time as the horizontal cracks at the mid-height of the wall, as they contributed to the formation of the overall out-of-plane mechanism of the wall.

8.3. Evolution of failure upon consecutive impacts

Fig. 16, Fig. 17 display the in-plane horizontal and vertical displacements, along with the out-of-plane displacements and the cracking originating in the back face of the walls W10 and W11. The maps were extracted from the first three tests that were conducted on these walls, at 30 ms after the initiation of the impact, in order to illustrate the evolution of failure upon consecutive hits. For brevity, here the focus is on W10, W11, and not on W9, because those walls were hit with the same impact configuration.

Repeated impacts appear to amplify the failure mechanisms initially observed on the undamaged walls, i.e., the vertical bending and the punching of the walls (Section 8.1). The

evolution of the former mechanism is characterized by an increase in deflections. As it is visible from the maps of vertical and out-of-plane displacements, the walls separated into two distinct regions and experienced rocking of progressively higher amplitude. The latter mechanism saw the gradual ejection of the middle brick and the adjacent ones, as it can be observed from the maps of out-of-plane displacement. In addition, brick dislocations dispatched over an increasingly larger area, which resulted in extensive cracking in the later impacts (see the maps of major strain in W10-3, W11-3). In parallel, the central region of the walls underwent a horizontal bending of increasing amplitude, as shown by the horizontal displacements of the walls.

8.4. Observed post-test damage

Fig. 18 complements Fig. 16, Fig. 17 by displaying the location and extension of damage that was observed on the left and front faces of the walls W10, W11 after each test. The plots are the result of a damage survey that was conducted by eye in order to gather evidence of failure on the faces of the wall, especially on those that were not monitored by the HS cameras.

Both cracking and crushing were observed on these faces for all tests. Cracking emerged in the central region of the walls, where the dislocations occurred, and was generated by the oscillations that followed the impacts. Crushing occurred only in the region of the impact. It initially generated in the middle brick, and, upon consecutive hits, it extended to the adjacent bricks. Visible from the surveys are also the cracks occurring between the first and last course of bricks and the RC slabs, contributing to the formation of the overall out-of-plane mechanism

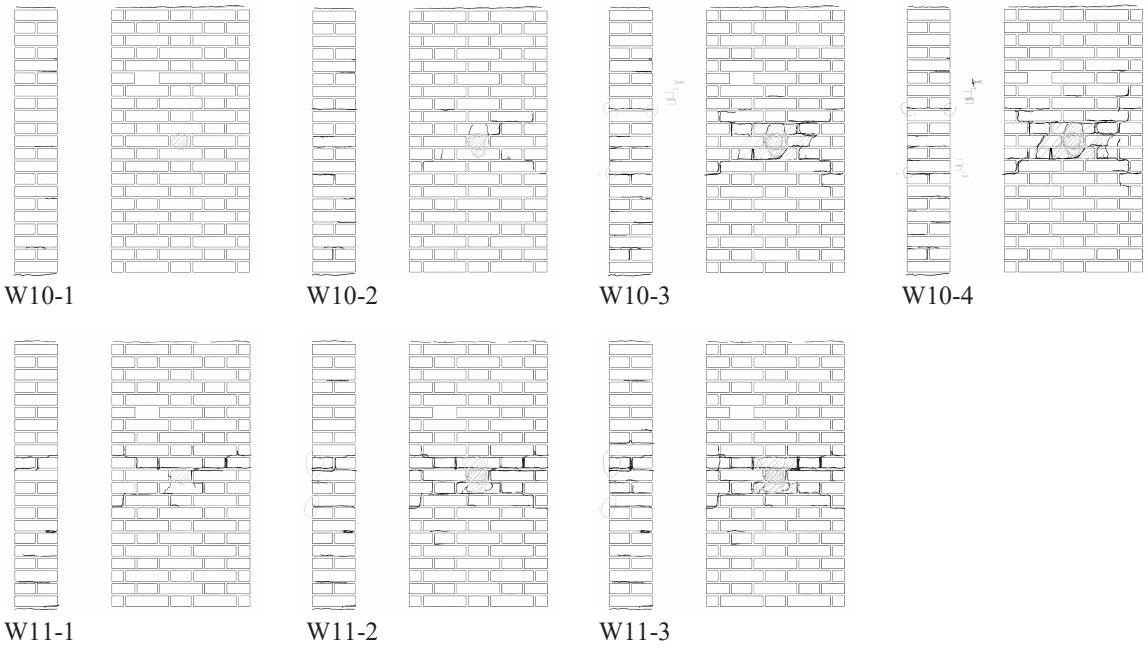

Fig. 18 Damage observed on the left and front faces of the walls after each test. Source: hand-annotated damage survey. Legend: black lines indicate visible cracks, with lines getting thicker as the cracks become larger; gray-shaded areas indicate regions where the masonry crushed, including those regions with no visible damage but that sounded hollow when knocking on the surface of the wall.

of the walls. In some tests, cracks could also be observed within the masonry units, as in the test W11-3. Moreover, in both walls, the middle brick split into two halves by a vertical crack located in the exact middle before being ejected.

8.5. Influence of axial load on the produced mechanisms

Wall W11 was characterized by a lower axial load than W10. Fig. 16-Fig. 18 yield a comparison between the mechanisms that generated in these walls.

The decrease in axial load put in place for W11 resulted in increased deflections, generating, since the early impacts, larger bending than in wall W10, both in the vertical and horizontal directions. This also resulted in an early ejection of the middle brick, and in a larger portion of wall to be ejected from wall W11 as compared to wall W10. The energy converted during the impacts was the same in both wall configurations. However, while in wall W11 a larger portion of energy was converted into kinetic energy and translated into deflection, in wall W10 such energy was dissipated mainly through cracking (Fig. 16, Fig. 17) and crushing (Fig. 18), because of the larger axial load to which the wall was subjected.

8.6. Wall deflections

Fig. 19 shows the records of the out-of-plane displacements of the walls (deflections) that were obtained by the 3D HS-DIC optical system. These measures were considered positive when in the direction of the impact. The plots include the displacements recorded at 2 points at the mid-height of the wall, namely, the central point of the 1st brick from the left and right-hand side of the walls, at about 50 mm from the wall's edges. The quantification of the displacement of the central point of the wall is only made for W9-1, W9-2, W9-3.

The wall deflections progressively increased as the impact occurred, reaching the peak positive value, d_{URM}, at the instant t_{URM}, and undergoing free oscillations once the impact was over. The values for d_{URM} and t_{URM} are listed in Table 4. The response of the left- and right-hand side of the walls appear to be fairly symmetric in all tests. In addition, the maximum deflections always occurred after the peak impact force was reached, $t_{\mathrm{URM}} \approx 0.52\Delta t_{\mathrm{imp}}$, which indicates that the impacts could induce the fast dynamic response of the walls. This also indicates that the maximum wall deflections occurred just before and, when the level of damage in the walls increased, in conjunction with the bouncing of the drop weight off the wall surface (c.f. t_{bounce} in Table 3). The wall deflection resulted, on average, in about twice the maximum displacement reached by the drop weight, $d_{\mathrm{URM}} \approx 2d_{\mathrm{bounce}}$. Finally, the ejection of the middle brick could be observed at the hit #4 for wall W10 and the hit #3 for wall W11, indicating the increased capacity of wall W10 to resist local impacts thanks to the higher axial load (Table 4).

8.7. Arching action

The forces measured by the force transducers varied during the impacts. The total resulting force corresponded, by the action-reaction principle, to a compression force applied to the top of the walls, i.e. the arching action. This latter is illustrated in Fig. 20 where, for comparison purposes, it is compared to the total force derived by the strain gauges. A correlation between the deformation of the rods and their force was assessed before the tests.

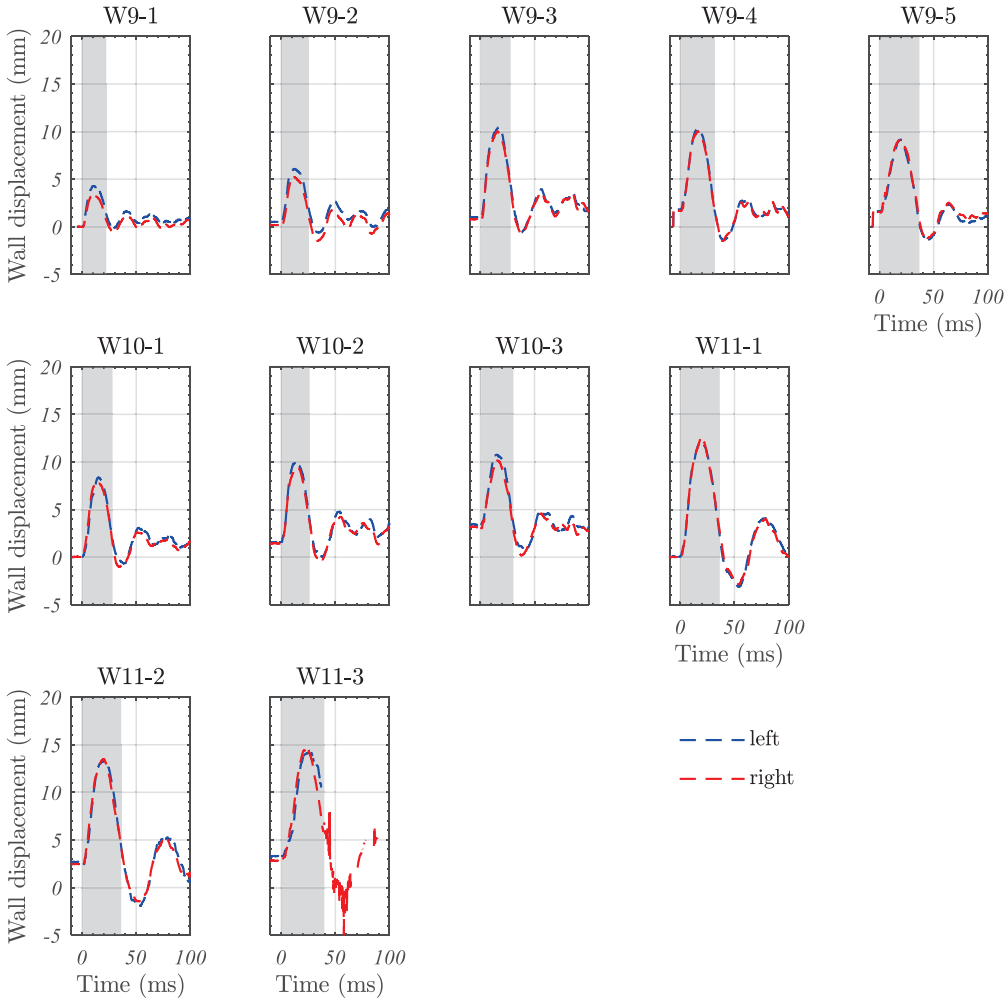

Fig. 19 Out-of-plane displacements of the walls at three points of the wall mid-height. Source: 3D HS-DIC measurements. Legend: gray-shaded areas indicate the interval when the impact occurred.

The forces recorded in the two steel rods were very similar during all impacts, which indicates that good symmetry between the left- and right-hand side of the walls was obtained in the test setup. However, in most of the tests their values tended to slightly differ after the impact. The arching action appears to progressively increase as the impact occurs, reaching the peak value, A_{peak}, at the instant t_{A} (Table 4). This occurred approximately when the maximum wall deflection was reached, on average $t_{\text{A}} \approx 0.52\Delta t_{\text{imp}}$, as a result of the non-rigid support conditions that were put in place for the upper RC slab, which resulted in an arching action proportional to the wall deflection. Finally, the forces derived from the strain gauges are in good agreement with those obtained by the force transducers, except for wall W10, where unintended damage in one measuring cable yielded inaccurate results.

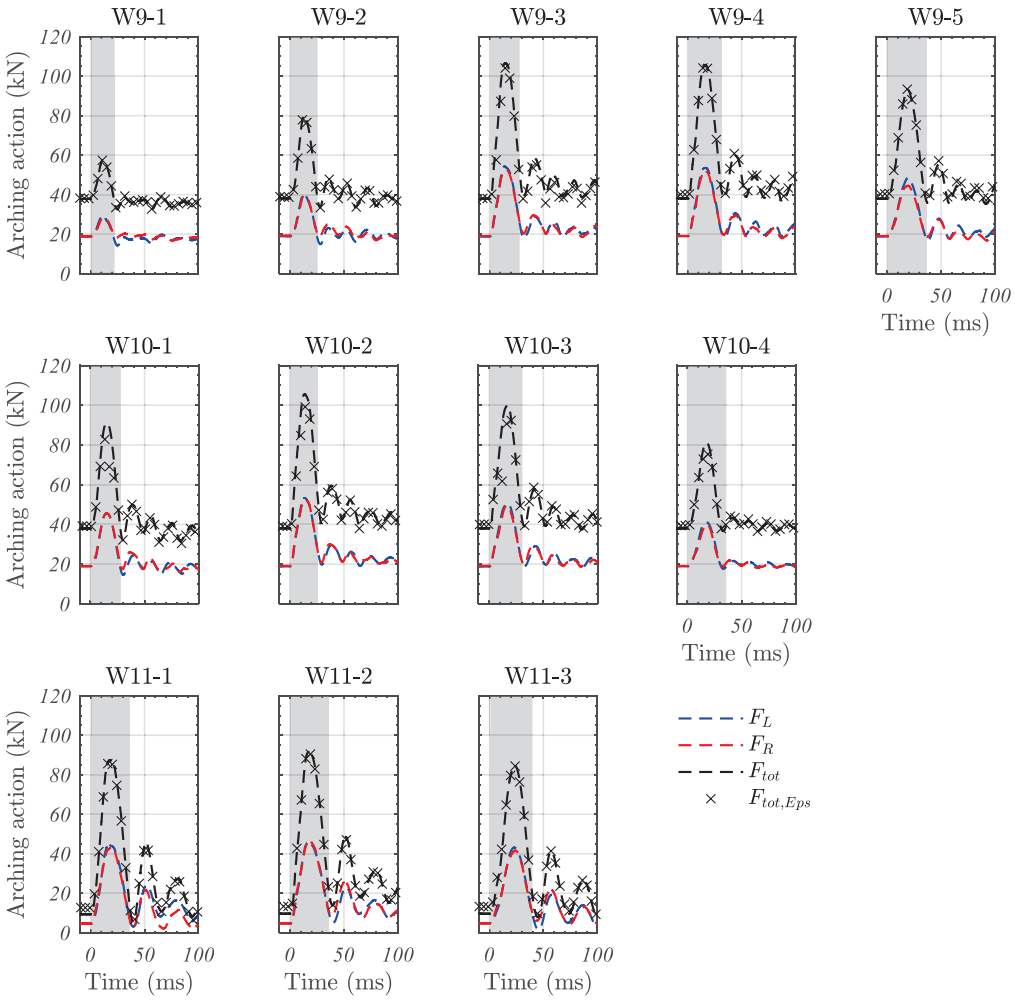

Fig. 20 Arching action. Source: force transducers (left, F_{L}, right, F_{R}, sum, F_{tot}), and strain gauges (sum, $F_{\mathrm{tot,Eps}}$). Legend: gray-shaded areas indicate the interval when the impact occurred. $F_{\mathrm{tot,Eps}}$ was downsampled for visualization purposes.

8.8. Wall uplift

Fig. 21 shows the records of the uplift experienced by the walls during the first 100 ms. The uplift corresponds here to the relative vertical displacement between the upper and lower RC slabs. It was obtained by multiplying the rods' deformation by their initial length (equal to the height of the wall). The bottom slab being fixed, a positive value of the uplift corresponds to an upward movement of the upper RC slab.

The uplifts that were recorded on the left- and right-hand sides of the walls were very close, meaning that very small in-plane rotations occurred in the upper RC slab. The uplift reaches its maximum, u_{peak}, at the instant t_{U}, which nearly corresponds to the instant t_{A} for the reasons

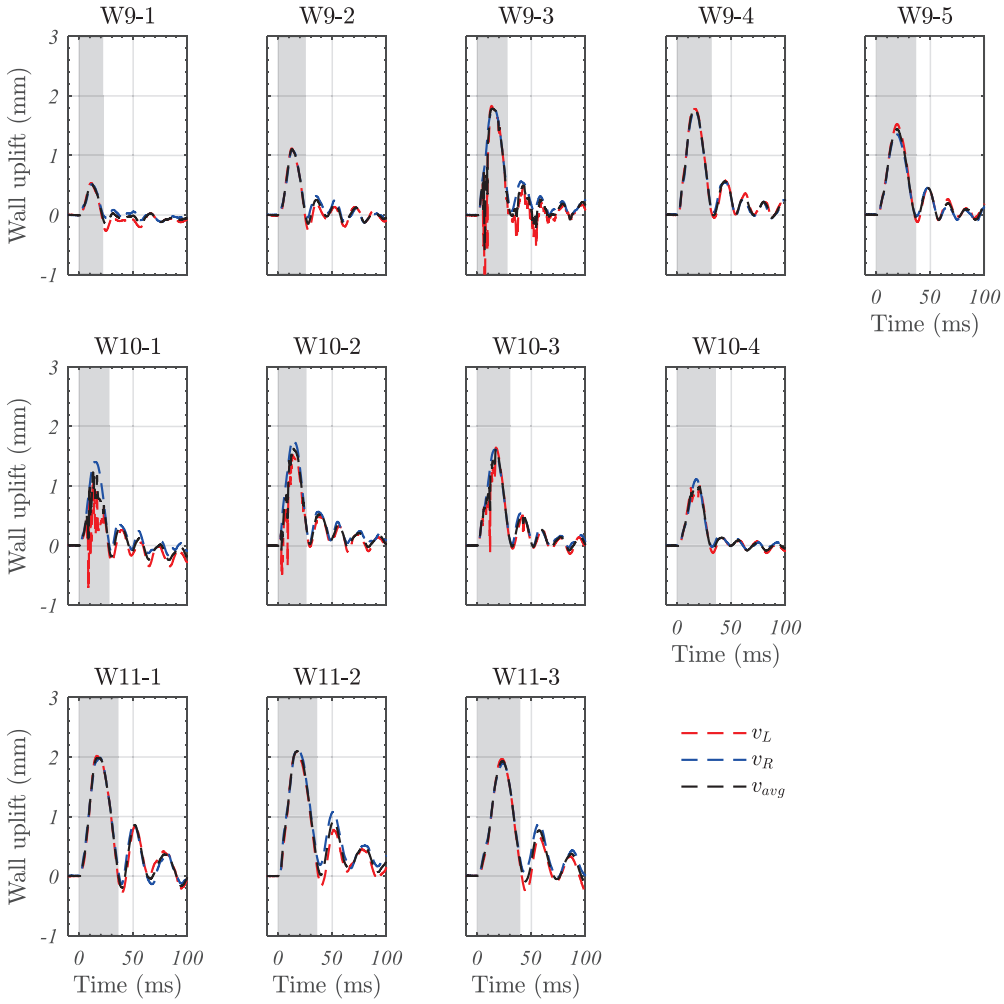

Fig. 21 Uplift of the wall top support. Source: strain gauges (mean of left gauges, v_{L}, mean of right gauges, v_{R}, total mean, v_{avg}). Legend: gray-shaded areas indicate the interval when the impact occurred.

explained in section 8.7 (Table 4).

9. Conclusions

The evaluation of the response of unreinforced brick masonry structures to blasts and impacts is cumbersome and requires advanced testing and modelling techniques [3]. The results of instrumented laboratory impact tests conducted on natural-scale double-wythe brick-mortar URM walls were discussed in this paper.

This research yielded two major contributions:

- The accurate observation of the response of brick URM walls subjected to slow-velocity

impacts, which included not only the wall deflections but also the evidence and development of failure, more particularly the initiation and propagation of cracking and crushing, the arise of arching action within the walls, and the uplift of the upper wall supports. This was documented for every impact and for two different wall configurations, where the initial axial load was varied.

- The development of an integrated experimental methodology based on optical measurements, making use of high-speed cameras and image correlation techniques (HS-DIC), to be used on URM walls subjected to impacts and, more generally, load scenarios characterized by relatively high loading rates.

More particularly, the following observations could be made.

Two combined failure mechanisms could be observed: the overall deflection of the walls on one hand, and the punching of the walls by the drop weight on the other.

During the first impacts, the undamaged walls suffered cracks on the back face that initiated directly behind the impact point, and radially propagated remote from this point. These cracks were concentrated in the central region of the walls, where brick dislocations occurred. Moreover, it could be observed that the maximum extent of cracking was generally produced in the walls approximately upon the reach of peak impact force.

The failure mechanisms initially observed on the undamaged walls amplified upon consecutive impact. On one hand, an increase in deflections was observed, because the walls separated into two distinct regions and experienced rocking of progressively higher amplitude. On the other hand, the middle brick and the adjacent ones tended to be ejected and brick dislocations dispatched over an increasingly larger area, which resulted in extensive cracking and crushing in the later impacts. In addition, the central region of the walls underwent a horizontal bending of increasing amplitude, this region not being laterally supported.

Table 4 Characterization of the wall response resulting from the pendulum tests.

Test	t_{URM} (left) (ms)	d_{URM} (left) (mm)	t_{URM} (right) (ms)	d_{URM} (right) (mm)	Brick ejection	t_A (ms)	A_{peak} (kN)	t_U (ms)	u_{peak} (mm)
W9-1	10.3	4.3	9.9	3.4	-	11.4	57.7	11.3	1.5
W9-2	11.6	6.1	11.2	5.4	-	12.6	80.1	12.5	2.1
W9-3	16.7	10.5	15.9	10.0	-	15.2	106.7	13.3	2.7
W9-4	16.2	10.3	16.2	10.0	-	15.3	105.8	15.7	2.8
W9-5	19.4	9.2	18.6	9.1	X	19.3	93.1	19.3	2.5
W10-1	15.1	8.4	14.7	7.8	-	14.9	91.1	12.8	2.2
W10-2	12.6	9.9	15.4	9.4	-	14.1	105.7	13.4	2.6
W10-3	14.7	10.8	15.5	10.2	-	16.9	99.9	16.9	2.6
W10-4	n/a	n/a	n/a	n/a	X	17.8	81.2	20.8	2.0
W11-1	18.9	11.9	19.9	12.5	-	18.4	87.6	17.5	2.3
W11-2	19.9	13.3	19.7	13.5	-	17.3	92.1	17.9	2.4
W11-3	25.7	14.4	24.1	14.6	X	23.2	84.8	23.5	2.2

The uplift and the arching action were measured for the first time in this campaign. It was shown that the arching increased upon wall deflection and reached its peak approximately when the maximum wall deflection was reached. The arching action was, at every instant, proportional to the uplift of the upper wall support, as a result of the non-rigid support conditions that were put in place for the walls.

The decreased axial load applied for one of the walls resulted in increased deflections which generated, since the early impacts, larger vertical and horizontal bending, an early ejection of the middle brick, and a larger portion of wall to be ejected from the wall. It could be deduced that, albeit the energy conveyed by the impacts was the same in both wall configurations, a larger portion of it was converted into kinetic energy (wall deflections) by the wall with smaller axial load, while the wall with higher axial load dissipated more energy through cracking and crushing and underwent smaller defections. This points at an increase in capacity to resist local impacts by URM walls subjected to higher initial axial loads. It is nonetheless worthwhile noticing that the axial loads applied to all tested walls were relatively low (axial load ratio < 5 %), and the conclusions drawn in this study hold true under these conditions. In fact, studies under static loading conditions indicate that higher axial loads may compromise the stability the walls, having a detrimental effect on the lateral wall capacity [36,37]. Further tests are needed to investigate this aspect under impact conditions.

When used with HS cameras, the DIC method proved itself a relevant tool for the observation and understanding of failure in URM walls subjected to impacts. This study proved the applicability and validated the use of these methods in laboratory conditions, on tests made on natural-scale small-size structural components. The experimental methodology developed here can now be applied to more complex test setups, components with larger geometry, and faster impact conditions.

Finally, the data generated in this study was made available [38] to support the development and validation of advanced numerical models for URM structures subjected to extreme actions.

Data and reproducibility

The test data discussed in this study are downloadable from the platform Zenodo, doi: 10.5281/zenodo.6838483 [38].

Acknowledgements

This study was funded by the ÅForsk Foundation, through the ‘Young researcher’ granting scheme, grant agreement n. 20-335.

References

[1] F. Masi, I. Stefanou, P. Vannucci, V. Maffi-Berthier, Rocking response of inverted pendulum structures under blast loading, International Journal of Mechanical Sciences. 157–158 (2019) 833–848. https://doi.org/10.1016/j.ijmecsci.2019.05.024.

[2] G. Michaloudis, N. Gebbeken, Modeling masonry walls under far-field and contact detonations, International Journal of Impact Engineering. 123 (2019) 84–97. https://doi.org/10.1016/j.ijimpeng.2018.09.019.

[3] M. Godio, N. Williams Portal, M. Flansbjer, J. Magnusson, M. Byggnevi, Experimental and numerical approaches to

investigate the out-of-plane response of unreinforced masonry walls subjected to free far-field blasts, Engineering Structures. 239 (2021) 112328. https://doi.org/10.1016/j.engstruct.2021.112328.

[4] F. Masi, I. Stefanou, P. Vannucci, A study on the effects of an explosion in the Pantheon of Rome, Engineering Structures. 164 (2018) 259–273. https://doi.org/10.1016/j.engstruct.2018.02.082.

[5] P.W. Sielicki, T. Łodygowski, Masonry wall behaviour under explosive loading, Engineering Failure Analysis. 104 (2019) 274–291. https://doi.org/10.1016/j.engfailanal.2019.05.030.

[6] H. Hao, B.G. Tarasov, Experimental Study of Dynamic Material Properties of Clay Brick and Mortar at Different Strain Rates, Australian Journal of Structural Engineering. 8 (2008) 117–132. https://doi.org/10.1080/13287982.2008.11464992.

[7] M. Gilbert, B. Hobbs, T.C.K. Molyneaux, The performance of unreinforced masonry walls subjected to low-velocity impacts: experiments, International Journal of Impact Engineering. 27 (2002) 231–251. https://doi.org/10.1016/S0734-743X(01)00049-5.

[8] M. Gilbert, B. Hobbs, T.C.K. Molyneaux, The performance of unreinforced masonry walls subjected to low-velocity impacts: mechanism analysis, International Journal of Impact Engineering. 27 (2002) 253–275. https://doi.org/10.1016/S0734-743X(01)00050-1.

[9] H. Jin, C. Sciammarella, S. Yoshida, L. Lamberti, Advancement of Optical Methods in Experimental Mechanics, Volume 3, 2016. https://doi.org/10.1007/978-3-319-00768-7.

[10] M.A. Sutton, J.-J. Orteu, H. Schreier, Image correlation for shape, motion and deformation measurements, Springer US, Boston, MA, 2009. https://doi.org/10.1007/978-0-387-78747-3.

[11] A.F. Cinar, S.M. Barhli, D. Hollis, M. Flansbjer, R.A. Tomlinson, T.J. Marrow, M. Mostafavi, An autonomous surface discontinuity detection and quantification method by digital image correlation and phase congruency, Optics and Lasers in Engineering. 96 (2017) 94–106. https://doi.org/10.1016/j.optlaseng.2017.04.010.

[12] A. Rezaie, M. Godio, K. Beyer, Investigating the cracking of plastered stone masonry walls under shear–compression loading, Construction and Building Materials. 306 (2021) 124831. https://doi.org/10.1016/j.conbuildmat.2021.124831.

[13] A. Rezaie, M. Godio, R. Achanta, K. Beyer, Machine-learning for damage assessment of rubble stone masonry piers based on crack patterns, Automation in Construction. 140 (2022) 104313. https://doi.org/10.1016/j.autcon.2022.104313.

[14] M. Flansbjer, N. Williams Portal, D. Vennetti, U. Mueller, Composite Behaviour of Textile Reinforced Reactive Powder Concrete Sandwich Façade Elements, International Journal of Concrete Structures and Materials. 12 (2018). https://doi.org/10.1186/s40069-018-0301-4.

[15] N. Williams Portal, M. Flansbjer, D. Honfi, Testing of self-supporting laminated glass balustrades, 2019. http://ri.diva-portal.org/smash/record.jsf?pid=diva2%3A1372865&dswid=4819.

[16] A.H. Salmanpour, N. Mojsilović, J. Schwartz, Displacement capacity of contemporary unreinforced masonry walls: An experimental study, Engineering Structures. 89 (2015) 1–16. https://doi.org/10.1016/j.engstruct.2015.01.052.

[17] N. Mojsilović, A.H. Salmanpour, Masonry walls subjected to in-plane cyclic loading: application of digital image correlation for deformation field measurement, International Journal of Masonry Research and Innovation. 1 (2016) 165. https://doi.org/10.1504/ijmri.2016.077473.

[18] N. Guerrero, M. Martínez, R. Picón, M.E. Marante, F. Hild, S. Roux, J. Flórez-López, Experimental analysis of masonry infilled frames using digital image correlation, Materials and Structures. 47 (2014) 873–884. https://doi.org/10.1617/s11527-013-0099-0.

[19] R. Ghorbani, F. Matta, M.A. Sutton, Full-Field Deformation Measurement and Crack Mapping on Confined Masonry Walls Using Digital Image Correlation, Experimental Mechanics. 55 (2015) 227–243. https://doi.org/10.1007/s11340-014-9906-y.

[20] C. Calderini, S. Degli Abbati, P. Cotič, M. Krzan, V. Bosiljkov, In-plane shear tests on masonry panels with plaster: correlation of structural damage and damage on artistic assets, Bulletin of Earthquake Engineering. 13 (2015) 237–256. https://doi.org/10.1007/s10518-014-9632-y.

[21] M. Bolhassani, A.A. Hamid, S. Rajaram, P.A. Vanniamparambil, I. Bartoli, A. Kontsos, Failure analysis and damage detection of partially grouted masonry walls by enhancing deformation measurement using DIC, Engineering Structures. 134 (2017) 262–275. https://doi.org/10.1016/j.engstruct.2016.12.019.

[22] R. el Nabouch, Q.B. Bui, O. Plé, P. Perrotin, Rammed earth under horizontal loadings: Proposition of limit states, Construction and Building Materials. 220 (2019) 238–244. https://doi.org/10.1016/j.conbuildmat.2019.06.020.

[23] H.L. Nghiem, M. al Heib, F. Emeriault, Method based on digital image correlation for damage assessment in masonry structures, Engineering Structures. 86 (2015) 1–15. https://doi.org/10.1016/j.engstruct.2014.12.021.

[24] N. Shetty, G. Livitsanos, N. van Roy, D.G. Aggelis, D. van Hemelrijck, M. Wevers, E. Verstrynge, Quantification of progressive structural integrity loss in masonry with Acoustic Emission-based damage classification, Construction and Building Materials. 194 (2019) 192–204. https://doi.org/10.1016/j.conbuildmat.2018.10.215.

[25] Y. Sieffert, F. Vieux-Champagne, S. Grange, P. Garnier, J.C. Duccini, L. Daudeville, Full-field measurement with a digital image correlation analysis of a shake table test on a timber-framed structure filled with stones and earth, Engineering Structures. 123 (2016) 451–472. https://doi.org/10.1016/j.engstruct.2016.06.009.

[26] S. Acikgoz, M.J. DeJong, K. Soga, Sensing dynamic displacements in masonry rail bridges using 2D digital image correlation, Structural Control and Health Monitoring. 25 (2018) 1–24. https://doi.org/10.1002/stc.2187.

[27] M. Dhanasekar, P. Prasad, J. Dorji, T. Zahra, Serviceability Assessment of Masonry Arch Bridges Using Digital Image Correlation, Journal of Bridge Engineering. 24 (2019) 1–16. https://doi.org/10.1061/(ASCE)BE.1943-5592.0001341.

[28] N. Williams Portal, M. Godio, M. Flansbjer, J. Magnusson, M. Byggnevi, Out-of-plane pushover tests on single- and double-wythe brick masonry walls instrumented with optical measurements: influence of local deformations and arching action on wall capacity, Under Preparation. (2022).

[29] Skellefteå Museum, Hålla hus - Tegel- och betongstommar, (2019). http://hallahus.se/renovera/stommen/tegel-och-betongstommar/murtegel/ (accessed December 2, 2019).

[30] EN 772-1, Methods of test for masonry units - Part 1: Determination of compressive strength, 2015.

[31] EN 1015-11, Methods of test for mortar for masonry - Part 11: Determination of flexural and compressive strength of hardened mortar, 2019.

[32] EN 1052-1, Methods of test for masonry - Part 1: Determination of compressive strength, 1992.

[33] M. Godio, F. Vanin, S. Zhang, K. Beyer, Quasi-static shear-compression tests on stone masonry walls with plaster: Influence of load history and axial load ratio, Engineering Structures. 192 (2019) 264–278. https://doi.org/10.1016/j.engstruct.2019.04.041.

[34] EN 1052-5, Methods of test for masonry - Part 5 : Determination of bond strength by the bond wrench method, 2005.

[35] US Department of Defense, UFC 3-340-02. Structures to resist the effects of the accidental explosions, 2008.

[36] M. Godio, K. Beyer, Analytical model for the out-of-plane response of vertically spanning unreinforced masonry walls, Earthquake Engineering & Structural Dynamics. 46 (2017) 2757–2776. https://doi.org/10.1002/eqe.2929.

[37] A.E. Schultz, J.G. Mueffelman, Elastic Stability of URM Walls Under Transverse Loading, TMS Journal (The Masonry Society). 21 (2003) 31–40.

[38] M. Godio, N. Williams Portal, M. Flansbjer, Experimental data: Slow-velocity out-of-plane impact tests on double-wythe unreinforced brick masonry walls instrumented with optical measurements, (2022). https://doi.org/10.5281/zenodo.6838483.

Appendix A. Acceleration records obtained by 2D HS-DIC

Acceleration-time records are key in characterizing the impact, because the force and impulse generated by the drop weight on the surface of the wall can be directly derived from those signals. The applicability of the optical measurements for obtaining these records as a proxy to hard-wired measurements is here assessed.

Fig. 22 superposes the records given by the accelerometers to those that were found by using the 2D HS-DIC.

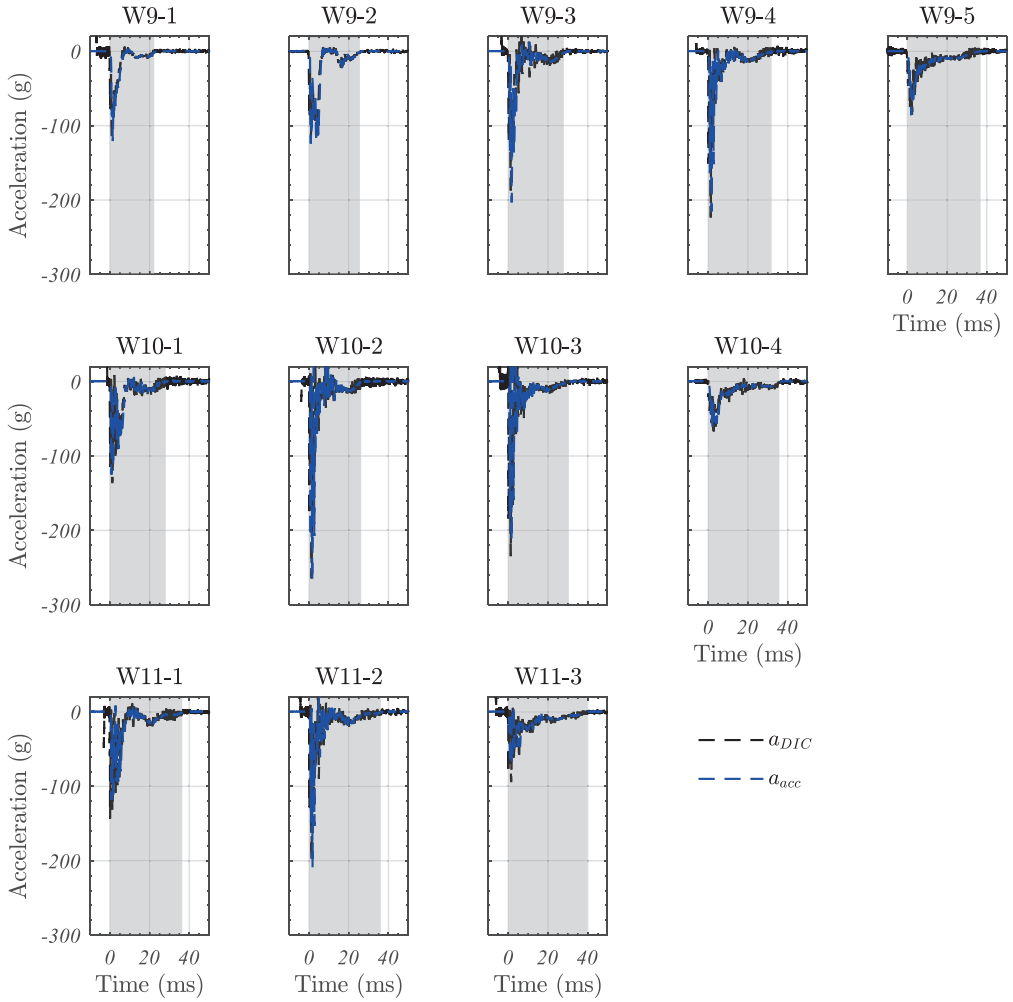

Fig. 22 Horizontal acceleration of the drop weight. Source: accelerometers (a_{acc}) and 2D HS-DIC (a_{DIC}). Legend: gray-shaded areas indicate the interval when the impact occurred.

The comparison is, in general, fairly satisfying. The signal provided by the 2D HS-DIC is only affected by some noise consisting in small-amplitude oscillations around the average value. However, these oscillations become particularly visible only before and after the impact, thus not affecting the main event. As a result, a similar error was obtained when using both signals for the integration of the impulse during the impact (Table 5), as compared to the impulse computed as momentum difference (see Section 7.3). A relatively larger, but still acceptable, difference was found in the peak accelerations recorded by said signals (Table 5). It is possible that such difference could be due to the different location of the sensors on the drop weight. Further investigation is therefore needed to corroborate this observation. Such oscillations may be filtered by applying, e.g, a low-pass filter at about 1500 Hz, or a least-squares moving average method, outside the region of the main signal event.

Table 5 Relative error committed by the accelerometers and 2D HS-DIC optical system in a) integrating the impulse (resp. I_{acc}, I_{DIC}) compared to the impulse computed as momentum difference (ΔP), and b) recording the peak accelerations (resp. $A_{\mathrm{peak,acc}}$, $A_{\mathrm{peak,DIC}}$).

Test	$\frac{(I_{acc} - \Delta P)}{\Delta P}$ (%)	$\frac{(I_{DIC} - \Delta P)}{\Delta P}$ (%)	$\frac{(A_{\mathrm{peak,DIC}} - A_{\mathrm{peak,acc}})}{A_{\mathrm{peak,acc}}}$ (%)
W9-1	1.95	-1.66	-4.88
W9-2	2.07	-2.13	-6.52
W9-3	1.53	-1.52	-5.74
W9-4	1.65	0.10	3.81
W9-5	2.71	-1.61	4.40
W10-1	0.51	-0.77	9.31
W10-2	-1.24	-1.59	-1.29
W10-3	-0.79	-0.27	9.82
W10-4	-1.35	-0.58	17.63
W11-1	-2.02	-1.66	21.25
W11-2	-1.83	-1.39	-4.82
W11-3	-1.91	0.14	35.79